Exploring muonphilic dark matter with the Z_2-even mediator at muon colliders*

Wanyun Chen (陈菀昀)[1,2] Haoqi Li (李皓奇)[1] Chih-Ting Lu (卢致廷)[1,3†] Qiulei Wang (王秋磊)[1]

[1]Department of Physics and Institute of Theoretical Physics, Nanjing Normal University, Nanjing 210023, China
[2]Department of Physics, Konkuk University, 120 Neungdong-ro, Gwangjin-gu, Seoul 05029, Korea
[3]Nanjing Key Laboratory of Particle Physics and Astrophysics, Nanjing 210023, China

Abstract: The Galactic Center GeV Excess (GCE) remains a compelling but enigmatic signal from the inner regions of our galaxy. Muonphilic dark matter (DM), which couples exclusively to muons via a new mediator, provides a viable explanation for the GCE and relic density while naturally evading constraints from direct detection, collider searches, and other multimessenger observations. Based on the viable nonresonant parameter space identified in previous global fits, we perform a comprehensive study on the prospects for discovering such muonphilic DM in the context of a future 3 TeV muon collider, focusing on simplified models with a Z_2-even mediator. Four distinct search strategies are investigated: visible on-shell mediator decays ($\mu^+\mu^-\gamma$ final state), invisible on-shell mediator decays (mono-photon plus missing energy), mono-photon production via off-shell mediators, and vector boson fusion production. Through a detailed signal-background analysis using cut-and-count methods, we project the exclusion limits at 95% confidence level for seven representative models across a wide range of mediator masses. Our results demonstrate that the projected limits cover a significant portion of viable parameter space that explains the GCE, establishing a muon collider as a decisive machine for testing the muonphilic DM hypothesis.

Keywords: dark matter, muon collider, beyond the Standard Model

DOI: 10.1088/1674-1137/ae5044 **CSTR:** 32044.14.ChinesePhysicsC.50063106

I. INTRODUCTION

Dark matter (DM) is a nonluminous form of matter that does not interact electromagnetically, yet its gravitational influence profoundly shapes the dynamics of galaxies and large-scale structures in the universe [1, 2]. As one of the most compelling pieces of evidence for physics beyond the Standard Model (SM), the existence of DM remains a major challenge to modern physics [3, 4]. Although DM constitutes approximately 27% of the total mass-energy content of the universe, compared to merely 5% from ordinary baryonic matter, its particle nature remains entirely unknown [5−9]. Long-standing anomalies in indirect DM detection, such as the Galactic Center GeV Excess (GCE) [10−12], antiproton excess [13−15], and the 511 keV [16−18] and 3.5 keV [10, 19] lines, have motivated extensive efforts to uncover potential connections to DM physics.

Among these indirect detection signals, the GCE, first identified by the Fermi-LAT satellite in 2009 [20−23], remains one of the most persistent and challenging puzzles in high-energy astrophysics and particle physics. This signal exhibits a significant gamma-ray excess in the 1–3 GeV range from the galactic center, with a spatial distribution consistent with the predicted Navarro–Frenk–White density profile of DM [24]. Its spectral shape also closely resembles expectations from weakly interacting massive particle (WIMP) annihilation channels, such as $b\bar{b}$ [21, 22]. However, secondary particles (*e.g.*, hadrons or electrons) produced in such annihilations would generate observable signals at other wavelengths (*e.g.*, radio or X-rays), although current multiwavelength observations have not yet confirmed such counterparts [25, 26].

Various DM models have been proposed to explain the GCE [27−42]. In recent years, muonphilic DM has emerged as a promising candidate owing to its consistency with multimessenger observational constraints [12, 40]. Conventional WIMP models, which remain leading explanations, involve annihilation into SM particles (*e.g.*,

Received 1 December 2025; Accepted 10 March 2026; Accepted manuscript online 11 March 2026

* Chih-Ting Lu, Wanyun Chen and Haoqi Li are supported by the National Natural Science Foundation of China (NNSFC) (12335005, 12575118) and the Special funds for postdoctoral overseas recruitment, Ministry of Education of China

† E-mail: 06285@njnu.edu.cn

$b\bar{b}$, $\tau^+\tau^-$, or W^+W^-), producing gamma rays via inverse Compton scattering or hadronization processes. However, such models face tensions with antiproton and positron spectra from AMS-02 [43, 44] and direct detection limits from experiments such as PandaX [45].

To resolve these tensions, muonphilic DM models have been proposed, which posit that DM couples exclusively to muon pairs ($\mu^+\mu^-$) via a mediator, with negligible interactions with other SM particles [40, 46–61]. This feature avoids hadronic or electronic secondary emission, offering a consistent explanation for the GCE without conflicting with other observational data. When DM particles annihilate into $\mu^+\mu^-$ or produce four muons via decays from a pair of mediators, final-state radiation (FSR) photons are generated predominantly in the 1–5 GeV range. The resulting spectrum exhibits a pronounced peak-like feature that aligns well with the GCE observed by Fermi-LAT [12, 40]. Compared with other channels (*e.g.*, $b\bar{b}$), the $\mu^+\mu^-$ final state yields a harder FSR spectrum with a steeper rise and sharper peak at approximately 1–3 GeV, making it ideal for reproducing the GCE spectral morphology [62, 63]. Furthermore, since the model couples only to muons, it avoids detectable synchrotron radiation from electrons/positrons or hadronic emission to evade constraints from radio (*e.g.*, WMAP/Planck synchrotron limits) and X-ray (e.g., Chandra inverse Compton bounds) observations [64–66]. This enables muonphilic DM models to resolve persistent multimessenger tensions that challenge conventional DM scenarios.

In muonphilic DM models, DM couples exclusively to muons via a mediator, such as a dark photon or scalar boson, making it challenging to probe at conventional colliders like the Large Hadron Collider (LHC) and Large Electron-Positron Collider (LEP) as well as direct detection experiments, which consequently impose weak constraints. However, owing to the muon's mass (approximately 200 times that of the electron) and its absence from strong interactions, a high-energy muon collider (at the TeV scale) offers superior energy resolution and cleaner backgrounds compared to hadron colliders (*e.g.*, LHC) or electron-positron colliders (*e.g.*, CEPC/FCC-ee) [67–69]. Thus, high-energy muon colliders represent a promising avenue for directly probing muonphilic DM[1)].

In this study, we investigate the following signal processes at a muon collider: (1) visible on-shell mediator decays: $\mu^+\mu^- \to \gamma + \text{MED}$ with $\text{MED} \to \mu^+\mu^-$, where MED denotes the mediator; (2) mono-photon with on-shell mediators: $\mu^+\mu^- \to \gamma + \text{MED}$ with $\text{MED} \to \chi\bar{\chi}$, where the DM particles (χ) yield missing energy and the photon energy distribution exhibits a peak-like structure; (3) mono-photon with off-shell mediators: $\mu^+\mu^- \to \gamma + \chi\bar{\chi}$, producing photon and missing energy signatures similar to SM backgrounds, thereby complicating signal extraction; and (4) vector boson fusion production: $\mu^+\mu^- \to \nu_\mu\bar{\nu}_\mu\mu^+\mu^-$ MED with $\text{MED} \to \mu^+\mu^-/\chi\bar{\chi}$. Using these search strategies, a muon collider can directly test whether muonphilic DM models resolve the longstanding GCE, precisely measure the DM-muon coupling strength and mediator mass, and complement the limitations of LHC searches and direct detection experiments. Combined with astrophysical observations from Fermi-LAT, AMS-02, and others, muon collider searches enable cross-validation of potential DM-induced astrophysical signals.

The remainder of this paper is organized as follows. Section II briefly reviews simplified muonphilic DM models ,and their key parameter space. Based on the allowed parameter space of muonphilic DM models, Section III proposes four search strategies and provides a state-of-the-art signal-background analysis. The resulting projected exclusion limits for muonphilic DM models at muon colliders are presented and discussed in Section IV, while Section V concludes. Collider constraints from LEP and LHC on muonphilic DM models are discussed in Appendix A.

II. SIMPLIFIED MUONPHILIC DM MODELS WITH THE Z_2-EVEN MEDIATOR

A. The models

For simplified muonphilic DM models consisting of an SM singlet DM particle and a mediator (MED), our previous work [40] systematically introduced all renormalizable interaction types: 16 in the Z_2-even mediator framework and 7 in the Z_2-odd mediator framework. These models are constructed from different spin and interaction combinations of DM and MED particles, with DM stability ensured by the Z_2 symmetry. Using a likelihood function incorporating experimental observations, including the Fermi-LAT GCE [63], Plank DM relic density [74], PandaX-4T direct detection limits [75], LEP collider bounds [76], and muon $g-2$ anomaly δa_μ [77], we performed a global analysis of all 23 interaction types to exclude parameter spaces inconsistent with observational data.

In Z_2-even mediator models, interactions between DM pairs and SM muon pairs are mediated by a Z_2-even SM singlet mediator with spin 0 or 1. Such muonphilic DM models naturally evade LEP and LHC constraints from mono-photon and monojet searches [78, 79], thus allowing for the existence of DM at the electroweak scale. Based on the spin and interaction types of DM and MED, the 16 Z_2-even interactions can be categorized in-

1) While several proposals exist to test DM models relevant to the GCE at colliders (see Refs. [28–32, 37, 70–73]), to the best of our knowledge, none have explored muonphilic DM models motivated by the GCE in the context of a muon collider, as investigated in this work.

to three major classes: (1) fermionic DM (χ) models, (2) scalar DM (S) models, and (3) vector DM (X_μ) models. When the DM mass (m_D) is less than the mediator mass (M), $m_D < M$, the observed relic density can only be achieved through the 2μ final state. For $m_D > M$, the process DM+DM $\rightarrow$ MED+MED becomes kinematically accessible, producing a 4μ final state. However, explaining the GCE in this case requires a significantly larger annihilation cross-section that typically conflicts with relic density constraints.

Z_2-even mediator models benefit from their ability to modulate early-time and present-day DM annihilation rates through an s-channel resonance enhancement mechanism ($M \approx 2m_D$), preserving the relic density while enhancing the GCE signal. For example, scalar mediator models ($\mathcal{L}_3$, $\mathcal{L}_9$, and $\mathcal{L}_{13}$) can simultaneously satisfy the relic density ($\langle\sigma v\rangle \approx 3\times10^{-26}$ cm^3/s) [74] and GCE signal ($\langle\sigma v\rangle \approx 4\times10^{-26}$ cm^3/s) [63] requirements by tuning the mediator decay width $\Gamma_{\rm MED}$ while explaining the muon $g-2$ anomaly ($\delta a_\mu \approx 2.51\times10^{-9}$) [77]. Moreover, the DM-nucleon scattering cross-sections are suppressed to $\sigma_{\rm SI} \sim 10^{-48}$ cm^2 owing to two-loop processes, evading current direct detection limits.

In contrast, Z_2-odd mediator models feature t-channel dominated DM annihilation. Since the mediator mass always exceeds the DM mass, the only accessible final state is 2μ, precluding the resonant enhancement mechanism available Z_2-even mediator models. This makes it challenging to simultaneously explain the GCE and DM relic abundance. In addition, the electrically charged nature of the mediator subjects it to LEP mass limits ($M > 103.5$ GeV) [76], significantly constraining the viable parameter space [40]. Satisfying the relic density requirement necessitates strong couplings ($g_D > 1$), which typically cause DM-nucleon scattering cross-sections to exceed current limits ($\sigma_{\rm SI} > 10^{-46}$ cm^2) [75]. In the end, the only Z_2-odd mediator model that marginally survives under thermal DM production is the vector DM model $\mathcal{L}_{23}$ ($g_D\bar{\psi}\gamma^\mu P_R \mu X_\mu^\dagger$); however, it requires $M > 300$ GeV and $g_D > 1.5$ to achieve the observed DM relic density. The parameter space is readily testable by LHC Run-3 data. Consequently, Z_2-odd mediator models do not possess a viable parameter space under current GCE, relic density, and direct detection constraints, while Z_2-even mediator models retain viable regions in both resonance and nonresonance regimes.

This study focuses on Z_2-even mediator models. The notations for relevant DM and MED candidates with various spin assignments are summarized in Table 1. We specifically explore the nonresonance regions of these muonphilic DM models in 3 TeV muon colliders [67]. The resonance regions are highly fine-tuned and sensitive to slight parameter variations within narrow parameter spaces, requiring specialized analysis that we defer to future work. Based on Table II and Fig. 3 of Ref. [40], we selected simplified DM models ($\mathcal{L}_3$, $\mathcal{L}_4$, $\mathcal{L}_8$, $\mathcal{L}_9$, $\mathcal{L}_{10}$, $\mathcal{L}_{13}$, and $\mathcal{L}_{14}$) with nonresonant parameter regions, as shown in Table 2. Here, g_D and $M_{D\phi}$ are relevant couplings between the mediator and a pair of DM particles that are dimensionless and one-dimensional, respectively. Similarly, g_f is the dimensionless coupling between the mediator and a pair of muons. Detailed expressions for DM annihilation and DM-nucleon scattering cross-sections are provided in our previous work [40].

Table 1. The dark matter and mediator notations used in this work.

	Scalar	Fermion	Vector
Dark Matter	S	χ	X^μ
Mediator	ϕ	ψ	V^μ

Table 2. The Lagrangian of relevant dark matter simplified models in the Z_2-even mediator scenario. Here, g_D and $M_{D\phi}$ are relevant couplings between the mediator and a pair of DM particles with dimensionless and dimension-1, respectively. Similarly, g_f is the dimensionless coupling between the mediator and a pair of muons.

Types	Lagrangian
χ and ϕ	$\mathcal{L}_3 = (g_D\bar{\chi}\mathrm{i}\gamma^5\chi + g_f\bar{f}f)\phi$
	$\mathcal{L}_4 = (g_D\bar{\chi}\mathrm{i}\gamma^5\chi + g_f\bar{f}\mathrm{i}\gamma^5 f)\phi$
χ and V_μ	$\mathcal{L}_8 = (g_D\bar{\chi}\gamma^\mu\chi + g_f\bar{f}\gamma^\mu\gamma^5 f)V_\mu$
S and ϕ	$\mathcal{L}_9 = (M_{D\phi}S^\dagger S + g_f\bar{f}f)\phi$
	$\mathcal{L}_{10} = (M_{D\phi}S^\dagger S + g_f\bar{f}\mathrm{i}\gamma^5 f)\phi$
X_μ and ϕ	$\mathcal{L}_{13} = (M_{D\phi}X^\mu X_\mu^\dagger + g_f\bar{f}f)\phi$
	$\mathcal{L}_{14} = (M_{D\phi}X^\mu X_\mu^\dagger + g_f\bar{f}\mathrm{i}\gamma^5 f)\phi$

B. The predicted parameter space

According to global fits in Ref. [40], only the simplified muonphilic DM models, $\mathcal{L}_3$, $\mathcal{L}_4$, $\mathcal{L}_8$, $\mathcal{L}_9$, $\mathcal{L}_{10}$, $\mathcal{L}_{13}$, and $\mathcal{L}_{14}$, exhibit allowed parameter space outside resonance regions[1)]. The parameter space can be further divided into two scenarios: $M > 2m_D$ and $M < 2m_D$. For $M > 2m_D$, on-shell mediator production is possible at muon colliders if kinematically accessible. The mediator may subsequently decay into either a DM particle pair or a muon pair, depending on the branching ratios. In contrast, for $M < 2m_D$, the mediator decays exclusively to muon pairs. DM particle pairs can only be produced via off-shell mediators, making their detection more challenging and strongly dependent on the ratio M/m_D. We therefore present this ratio for the relevant DM models in Fig. 1, based on results from Ref. [40]. We observe that

1) Here we do not consider the $\mathcal{L}_6$ case, as it only permits very light mediators outside the resonance region.

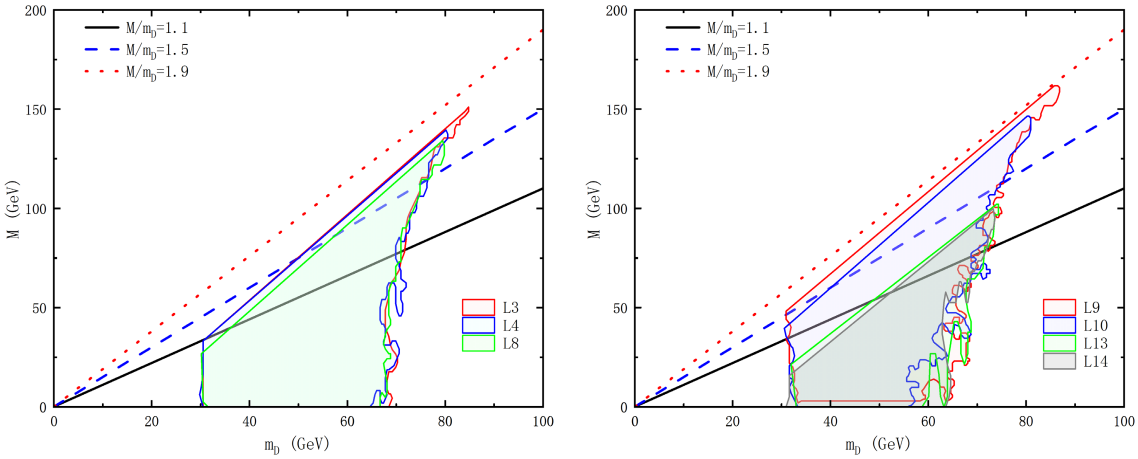

Fig. 1. (color online) Parameter space for relevant simplified muonphilic DM models with $M < 2m_D$, based on Ref. [40].The left panel depicts $\mathcal{L}_3$, $\mathcal{L}_4$ and $\mathcal{L}_8$, while the right panel covers $\mathcal{L}_9$, $\mathcal{L}_{10}$, $\mathcal{L}_{13}$ and $\mathcal{L}_{14}$. For comparison, three benchmark ratios of the mediator to DM mass are displayed: $M/m_D = 1.1$ (black-solid), $M/m_D = 1.5$ (blue-dashed), and $M/m_D = 1.9$ (red-dotted).

only models $\mathcal{L}_9$ and $\mathcal{L}_{10}$ feature parameter space near $M/m_D = 1.9$. The parameter spaces of $\mathcal{L}_3$, $\mathcal{L}_4$, and $\mathcal{L}_8$ approach the ratio $M/m_D = 1.5$, while $\mathcal{L}_{13}$ and $\mathcal{L}_{14}$ exhibit relatively small regions near $M/m_D = 1.1$.

Note that for a very light mediator ($M/m_D \ll 1$), fixed-target experiments are generally more efficient than muon colliders in searching for its visible on-shell decays. In this regime, aside from MED $\to \mu^+\mu^-$ at the tree level, other decay channels such as MED $\to e^+e^-, \gamma\gamma, \nu\bar{\nu}$ arise at loop level and depend on UV-completion details that lie beyond the scope of this work. Therefore, we restrict our discussion to mediator masses $M > 2m_\mu$, ensuring that the decay into a muon pair is kinematically allowed. Such light mediators can be searched for at BaBar and Belle II experiments [80, 81]. The NA64μ experiment is also sensitive to light muonphilic mediators [82, 83]; however, it primarily targets missing-momentum signatures from invisible decays, treating muon final states as backgrounds to be suppressed by veto systems [84]. Although NA64μ has set constraints on muonphilic DM in the $L_\mu - L_\tau$ model framework—retaining a unique sensitivity to invisible decays, where the mediator decays predominantly to DM pairs or neutrinos—the scenario studied here does not fall into that category. Instead, our work provides a complementary probe at future high-energy muon colliders.

This study focuses on three distinct types of searches for muonphilic DM models at muon colliders.

• Visible on-shell mediator decays

The mediator is produced on-shell at muon colliders and subsequently decays to a muon pair: $\mu^+\mu^- \to \gamma$, MED $\to \gamma(\mu^+\mu^-)$. The production cross-section depends only on g_f:

$$\sigma(\mu^+\mu^- \to \gamma, \text{MED}) \propto g_f^2, \tag{1}$$

while the branching ratio $\mathcal{B}(\text{MED} \to \mu^+\mu^-)$ is a function of g_f, g_D, and m_D.

• Invisible on-shell mediator decays

We consider the mono-photon signature in the regime where $M > 2m_D$ with $m_D < 100$ GeV, and where the couplings satisfy $g_D \cdot g_f \gtrsim 10^{-2}$ for models $\mathcal{L}_3$, $\mathcal{L}_4$, and $\mathcal{L}_8$, or $M_{D\phi} \cdot g_f \gtrsim 10^{-4}$ TeV for models $\mathcal{L}_9$, $\mathcal{L}_{10}$, $\mathcal{L}_{13}$, and $\mathcal{L}_{14}$.

• Mono-photon with off-shell mediators

We study the parameter region where $1.1m_D \lesssim M \lesssim 1.9m_D$ with $m_D < 100$ GeV, and with coupling constraints $g_D \cdot g_f \gtrsim 10^{-2}$ for $\mathcal{L}_3$, $\mathcal{L}_4$, and $\mathcal{L}_8$, and $M_{D\phi} \cdot g_f \gtrsim 10^{-4}$ TeV for $\mathcal{L}_9$, $\mathcal{L}_{10}$, $\mathcal{L}_{13}$, and $\mathcal{L}_{14}$.

III. MUONPHILIC DM SEARCH STRATEGIES AT MUON COLLIDERS

Based on the structure of the parameter space, we develop four distinct search strategies for muonphilic DM models at muon colliders: visible on-shell mediator decays (Section III.A), invisible on-shell mediator decays (Section III.B), mono-photon signatures with off-shell mediators (Section III.C), and vector boson fusion production (Section III.D). In the following subsections, we employ the following computational pipeline: `FeynRules` [85] generates UFO model files for the Lagrangians listed in Table 2; `MadGraph5_aMC@NLO` [86] produces Monte Carlo events for signal and background hard processes; `Pythia8` [87] handles parton showering and hadronization; and `Delphes3` [88] with a muon collider template performs fast detector simulation. We have also performed a simplified analysis of collider constraints from the LEP and LHC, with the corresponding details provided in Appendix A. These constraints, however, are

considerably weaker than those obtained in future muon colliders, which are the primary focus of this work.

A. Visible on-shell mediator decays

Figure 3 in Ref. [40] indicates that allowed parameter spaces exist outside resonance regions for models $\mathcal{L}_3, \mathcal{L}_4, \mathcal{L}_8, \mathcal{L}_9, \mathcal{L}_{10}, \mathcal{L}_{13}$, and $\mathcal{L}_{14}$. However, when considering on-shell mediator production through the visible decay channel $\mu^+\mu^- \to \gamma\text{MED}$ followed by $\text{MED} \to \mu^+\mu^-$, only three interaction types for the mediators and a pair of muons emerge: scalar ($\mathcal{L}_3, \mathcal{L}_9, \mathcal{L}_{13}$), pseudoscalar ($\mathcal{L}_4, \mathcal{L}_{10}, \mathcal{L}_{14}$), and axial-vector ($\mathcal{L}_8$). For the proposed 3 TeV muon collider, we focus on mediator masses $M < 1.5$ TeV, covering all upper bounds of mediator masses in these models except $\mathcal{L}_9$ and $\mathcal{L}_{10}$, where M may reach 3 TeV. Our search strategies remain extensible to heavier mediators for higher-energy muon colliders.

In this subsection, we demonstrate our methodology using the $\mathcal{L}_3$ and $\mathcal{L}_8$ models, presenting benchmark points (BPs), kinematic distributions, and event selection criteria. The analysis for other models is presented in Sec. IV. Note that for $M > 2m_D$, kinematically allowed invisible mediator decays lead to model-dependent variations in the $\text{MED} \to \mu^+\mu^-$ branching ratios. Therefore, we set the mass ratio $M/m_D = 2.5$ and fix the coupling constant ratio for each model, thereby ensuring that the branching ratio of $\text{MED} \to \mu^+\mu^-$ is no less than 99%. Four benchmark mediator masses are considered in this study: (1) Signal-1: $M = 50$ GeV; (2) Signal-2: $M = 500$ GeV; (3) Signal-3: $M = 900$ GeV; (4) Signal-4: $M = 1300$ GeV. For the $\mathcal{L}_3$ model, the benchmark coupling parameters are set to $g_f = 0.08$ and $g_D = 0.01$, corresponding to a coupling constant ratio of $g_D/g_f = 1/8$. For the $\mathcal{L}_8$ model, the benchmark coupling parameters are set to $g_f = 0.09$ and $g_D = 0.01$, with the corresponding coupling constant ratio being $g_D/g_f = 1/9$. For the signal process $\mu^+\mu^- \to \gamma\text{MED}$ with $\text{MED} \to \mu^+\mu^-$, the irreducible SM background process is $\mu^+\mu^- \to \mu^+\mu^-\gamma$[1)]. The corresponding production cross-sections for the four BPs and the SM background are listed in the second row of Tables 3 and 4. Representative kinematic distributions for signal and background processes are shown in Fig. 2.

We find that the peak of the background photon energy $E(\gamma)$ appears at 50 GeV, while the peaks for the four signal BPs occur at higher energies and decrease with increasing mediator mass, as shown in the top-left panel of Fig. 2. The photon pseudorapidity $\eta(\gamma)$ for the background and the light mediator case (signal-1) displays a pronounced forward-backward distribution. However, this behavior does not appear for heavier mediators, resulting in a flatter $\eta(\gamma)$ distribution (top-right panel). A similar forward-backward distribution is also observed in the $\eta(\mu^\pm)$ variable for both the background and signal-1 (middle-left panel). The transverse momentum distribution $p_T(\mu^-)$ peaks at approximately 350 GeV for the background. For the signal processes, a heavier mediator leads to a harder $p_T(\mu^-)$ spectrum (middle-right panel). The opening angle distribution $\Delta R(\mu^+\mu^-)$ provides a key distinction: a light mediator (signal-1) is produced with a large boost, leading to a smaller $\Delta R(\mu^+\mu^-)$ compared with the background. The background exhibits a significantly larger $\Delta R(\mu^+\mu^-)$ than all four signal BPs (bottom-left panel). Finally, the dimuon invariant mass distributions $M(\mu^+\mu^-)$ for the signals peak at their respective mediator masses, while the background distribution is broad and featureless (bottom-right panel).

Based on the above analysis of kinematic distributions, the following event selection criteria for signal and background events are adopted:

- Cut-1 (basic cuts): $N(\gamma), N(\mu^+), N(\mu^-) > 0$, with leading photon, a pair of muons satisfying $E(\gamma), p_T(\mu^\pm) > 20$ GeV, and $|\eta(\gamma)|, |\eta(\mu^\pm)| < 2.5$;
- Cut-2: $E(\gamma) > 150$ GeV, and $|\eta(\gamma)| < 1.8$;
- Cut-3: $p_T(\mu^\pm) > 150$ GeV, and $|\eta(\mu^\pm)| < 1.6$;
- Cut-4: $\Delta R(\mu^+\mu^-) < 3.0$;
- Cut-5: $|M(\mu^+\mu^-) - M| < 0.15M$.

After applying these selection criteria, the signal and background efficiencies are calculated. Tables 3 and 4 summarize the selection efficiencies for the four BPs in the $\mathcal{L}_3$ and $\mathcal{L}_8$ models, respectively. The final background efficiency is suppressed to $O(10^{-3})$, while the signal efficiencies remain above 19% and can exceed 40% for larger mediator masses.

B. Invisible on-shell mediator decays

The global fitting results from Fig. 3 of Ref. [40] show $M > 2m_D$ with $m_D < 100$ GeV. With the exception of models $\mathcal{L}_9$ and $\mathcal{L}_{10}$, where the mediator masses M can reach the upper bounds of 3 TeV, all other models ($\mathcal{L}_3$, $\mathcal{L}_4$, $\mathcal{L}_8$, $\mathcal{L}_{13}$, and $\mathcal{L}_{14}$) exhibit upper bounds of M below 1.5 TeV. Given our focus on the 3 TeV muon collider proposal, we restrict our study to mediator masses $M \lesssim 1.5$ TeV. Notably, on-shell mediator production via muon pairs occurs through scalar-type couplings ($\mathcal{L}_3$, $\mathcal{L}_9$, and $\mathcal{L}_{13}$), pseudoscalar-type couplings ($\mathcal{L}_4$, $\mathcal{L}_{10}$, and $\mathcal{L}_{14}$), or axial vector-type couplings ($\mathcal{L}_8$). However, branching ratios for mediator decays to DM particle pairs vary across models owing to their distinct interaction

1) The relevant VBF background processes including $\mu^+\mu^- \to \mu^+\nu_\mu\gamma W^-$, with $W^- \to \mu^-\bar{\nu}_\mu$, and $\mu^+\mu^- \to \mu^-\bar{\nu}_\mu\gamma W^+$, with $W^+ \to \mu^+\nu_\mu$ are also considered. However, these backgrounds have negligible impact on the final exclusion results, and their contributions can be safely neglected.

Table 3. Cut-flow table for visible on-shell mediator decays of the $\mathcal{L}_3$ model and its relevant background with cumulative efficiencies from **Cut-1** to **Cut-5**. The four benchmark points are signal-1 ($M = 50$ GeV), signal-2 ($M = 500$ GeV), signal-3 ($M = 900$ GeV), and signal-4 ($M = 1300$ GeV).

	Cut description	background	signal1	signal2	signal3	signal4
	Cross-section/fb	179	3.628	4.935	5.471	6.366
Cut-1	$N(\gamma), N(\mu^+), N(\mu^-) > 0,\ E(\gamma), p_T(\mu^\pm) > 20\,\text{GeV},\ \lvert\eta(\gamma)\rvert, \lvert\eta(\mu^\pm)\rvert < 2.5$	0.82	0.78	0.85	0.84	0.83
Cut-2	$E(\gamma) > 150\,\text{GeV},\ \lvert\eta(\gamma)\rvert < 1.8$	0.19	0.54	0.65	0.62	0.61
Cut-3	$p_T(\mu^\pm) > 150\,\text{GeV},\ \lvert\eta(\mu^\pm)\rvert < 1.6$	0.08	0.41	0.53	0.51	0.51
Cut-4	$\Delta R(\mu^+\mu^-) < 3.0$	0.01	0.24	0.40	0.46	0.45
Cut-5	$\lvert M(\mu^+\mu^-) - M\rvert < 0.15M$	2×10^{-5}	0.23	/	/	/
		3.7×10^{-4}	/	0.38	/	/
		1.34×10^{-3}	/	/	0.44	/
		2.15×10^{-3}	/	/	/	0.45

Table 4. Similar to Table 3, but for the $\mathcal{L}_8$ model.

	Cut description	background	signal1	signal2	signal3	signal4
	Cross-section/fb	179	7.99	10.08	11.43	13.89
Cut-1	$N(\gamma), N(\mu^+), N(\mu^-) > 0,\ E(\gamma), p_T(\mu^\pm) > 20\,\text{GeV},\ \lvert\eta(\gamma)\rvert, \lvert\eta(\mu^\pm)\rvert < 2.5$	0.82	0.77	0.85	0.84	0.83
Cut-2	$E(\gamma) > 150\,\text{GeV},\ \lvert\eta(\gamma)\rvert < 1.8$	0.19	0.53	0.60	0.59	0.58
Cut-3	$p_T(\mu^\pm) > 150\,\text{GeV},\ \lvert\eta(\mu^\pm)\rvert < 1.6$	0.08	0.40	0.47	0.46	0.48
Cut-4	$\Delta R(\mu^+\mu^-) < 3.0$	0.01	0.20	0.32	0.40	0.41
Cut-5	$\lvert M(\mu^+\mu^-) - M\rvert < 0.15M$	2×10^{-5}	0.19	/	/	/
		3.7×10^{-4}	/	0.31	/	/
		1.34×10^{-3}	/	/	0.39	/
		2.15×10^{-3}	/	/	/	0.40

types.

To demonstrate our search methodology, we use the $\mathcal{L}_3$ model as a representative example, presenting BPs, kinematic distributions, and event selection criteria. The analysis is subsequently extended to other models. We select four mediator masses: Signal-1 ($M = 50$ GeV), signal-2 ($M = 500$ GeV), signal-3 ($M = 900$ GeV), and signal-4 ($M = 1300$ GeV), with a fixed mediator-to-DM mass ratio $M/m_D = 2.5$, and choose $g_D = 0.15$ and $g_f = 0.01$ as our benchmark couplings. The signal process is $\mu^+\mu^- \to \phi\gamma$, followed by the on-shell mediator decay to a pair of DM particles ($\phi \to \chi\bar{\chi}$). The irreducible SM background process is $\mu^+\mu^- \to \nu\bar{\nu}\gamma$[1)]. The corresponding production cross-sections for the four BPs and the SM background are listed in the second row of Table 5. The representative kinematic distributions for signal and background processes are shown in Fig. 3.

For on-shell mediator production with an initial state radiation photon, the photon energy $E(\gamma)$ exhibits a monochromatic peak, while the background $E(\gamma)$ distribution decreases smoothly, as shown in the top-left panel of Fig. 3. The transverse missing energy $\not{E}_T$ is more energetic for signals than for background (top-right panel). Conversely, the missing energy $\not{E}$ distribution shows the opposite trend to $E(\gamma)$ distribution (bottom-left panel). Finally, since the photon transverse momentum and missing energy distributions differ significantly between signals and background, we examine the ratio $P_T(\gamma)/\not{E}$ distribution (bottom-right panel) to enhance discrimination.

Based on these kinematic distributions, we implement the following event selections to signal and background events:

- Cut-1 (basic cuts): $N(\gamma) > 0$, with the leading photon satisfying $E(\gamma) > 100\,\text{GeV}$ and $\lvert\eta(\gamma)\rvert < 2.5$, plus $\not{E}_T > 40\,\text{GeV}$;
- Cut-2: $E(\gamma) > 1200\,\text{GeV}$;
- Cut-3: $P_T(\gamma)/\not{E} > 0.4$;

1) Similarly, we have considered the relevant VBF process $\mu^+\mu^- \to \nu_\mu\bar{\nu}_\mu\gamma Z$, with $Z \to \nu_\ell\bar{\nu}_\ell$, but its contribution is highly suppressed and can be neglected in this analysis.

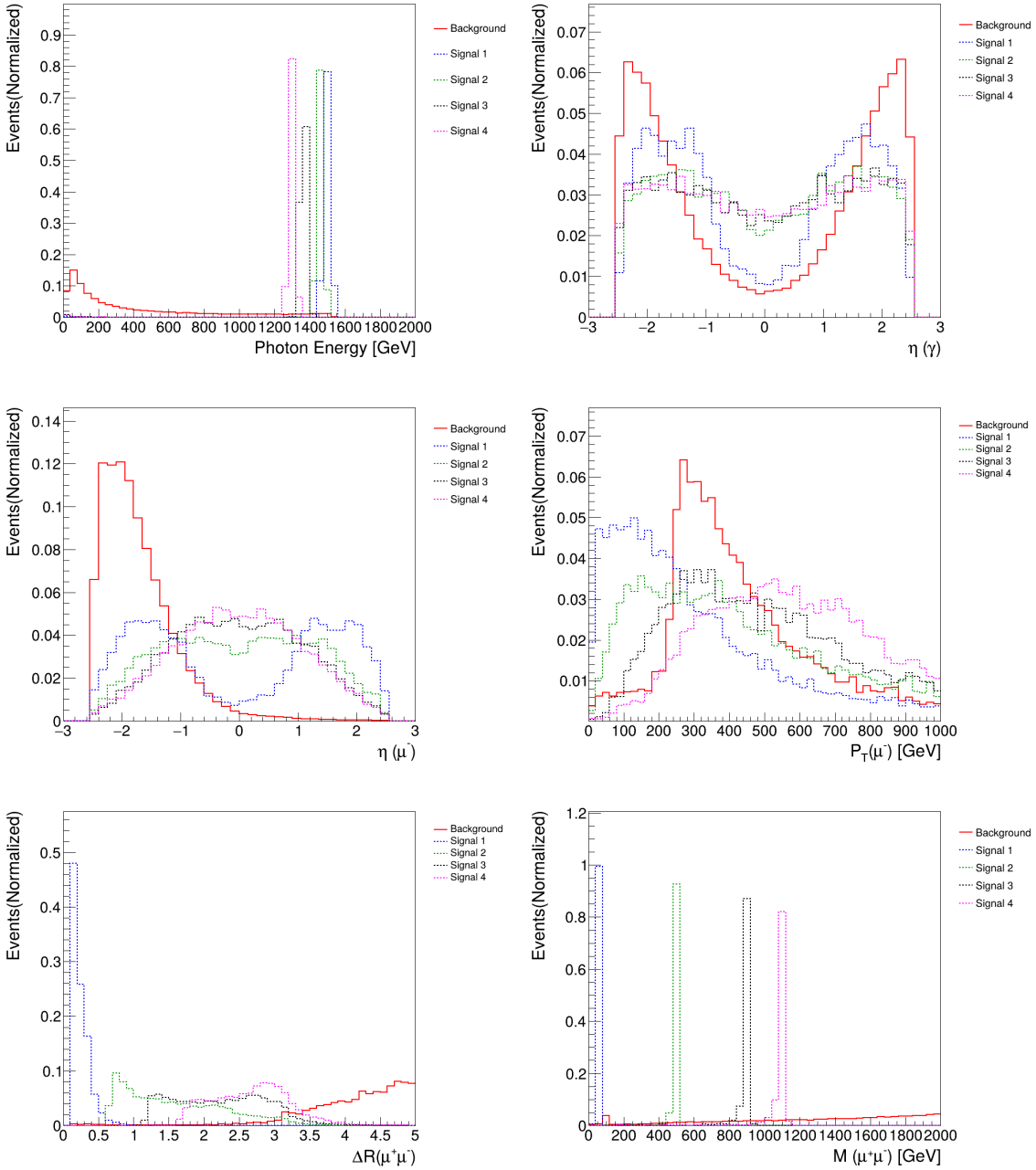

Fig. 2. (color online) Visible on-shell mediator decays of the $\mathcal{L}_3$ model. Representative kinematic distributions include photon energy $E(\gamma)$ (top-left), photon pseudorapidity $\eta(\gamma)$ (top-right), μ^- pseudorapidity $\eta(\mu^-)$ (middle-left), μ^- transverse momentum $p_T(\mu^-)$ (middle-right), ΔR of a muon pair (bottom-left), and invariant mass $M(\mu^+\mu^-)$ of a muon pair (bottom-right) for signal-1 ($M = 50$ GeV, blue-dotted line), signal-2 ($M = 500$ GeV, green-dotted line), signal-3 ($M = 900$ GeV, black-dotted line), signal-4 ($M = 1300$ GeV, purple-dotted line), and the background (red-solid line).

● Cut-4: $M_T > 1600$ GeV, where the transverse mass for the mono-photon plus $\not{E}_T$ is defined as

$$M_T = \sqrt{2P_T(\gamma)\cdot\not{E}_T\cdot(1-\cos\Delta\phi)}, \tag{2}$$

with $\Delta\phi$ being the azimuthal angle between the leading photon and $\not{E}_T$.

The final M_T selection is used to further distinguish signal and background events. Table 5 summarizes the selection efficiencies for four signal BPs in the $\mathcal{L}_3$ model and background. Because the efficiency table for the $\mathcal{L}_4$ model closely resembles that of the $\mathcal{L}_3$ model, we show only the $\mathcal{L}_8$ model in Table 6. We adopt the benchmark couplings of $g_D = 1.2$ and $g_f = 0.1$ in the $\mathcal{L}_8$ model.

Table 5. Cut-flow table for the invisible on-shell mediator decay scenario ($M/m_D = 2.5$) of the $\mathcal{L}_3$ model and its relevant background with cumulative efficiencies from **Cut-1** to **Cut-4**. The four benchmark points are signal-1 ($M = 50$ GeV), signal-2 ($M = 500$ GeV), signal-3 ($M = 900$ GeV), and signal-4 ($M = 1300$ GeV).

	Cut description	background	signal1	signal2	signal3	signal4
	Cross-section/fb	2980	8.21×10^{-2}	8.46×10^{-2}	9.10×10^{-2}	0.10
	$N(\gamma) > 0$	0.92	0.91	0.91	0.91	0.91
Cut-1	$E(\gamma) > 100\,\text{GeV}$ & $\lvert\eta(\gamma)\rvert < 2.5$	0.35	0.91	0.91	0.91	0.91
	$\not{E}_T > 40\,\text{GeV}$	0.30	0.91	0.91	0.91	0.91
Cut-2	$E(\gamma) > 1200\,\text{GeV}$	7.4×10^{-3}	0.91	0.91	0.91	0.83
Cut-3	$P_T(\gamma)/\not{E} > 0.4$	1.7×10^{-3}	0.57	0.56	0.51	0.38
Cut-4	$M_T > 1600\,\text{GeV}$	1.0×10^{-3}	0.45	0.45	0.42	0.32

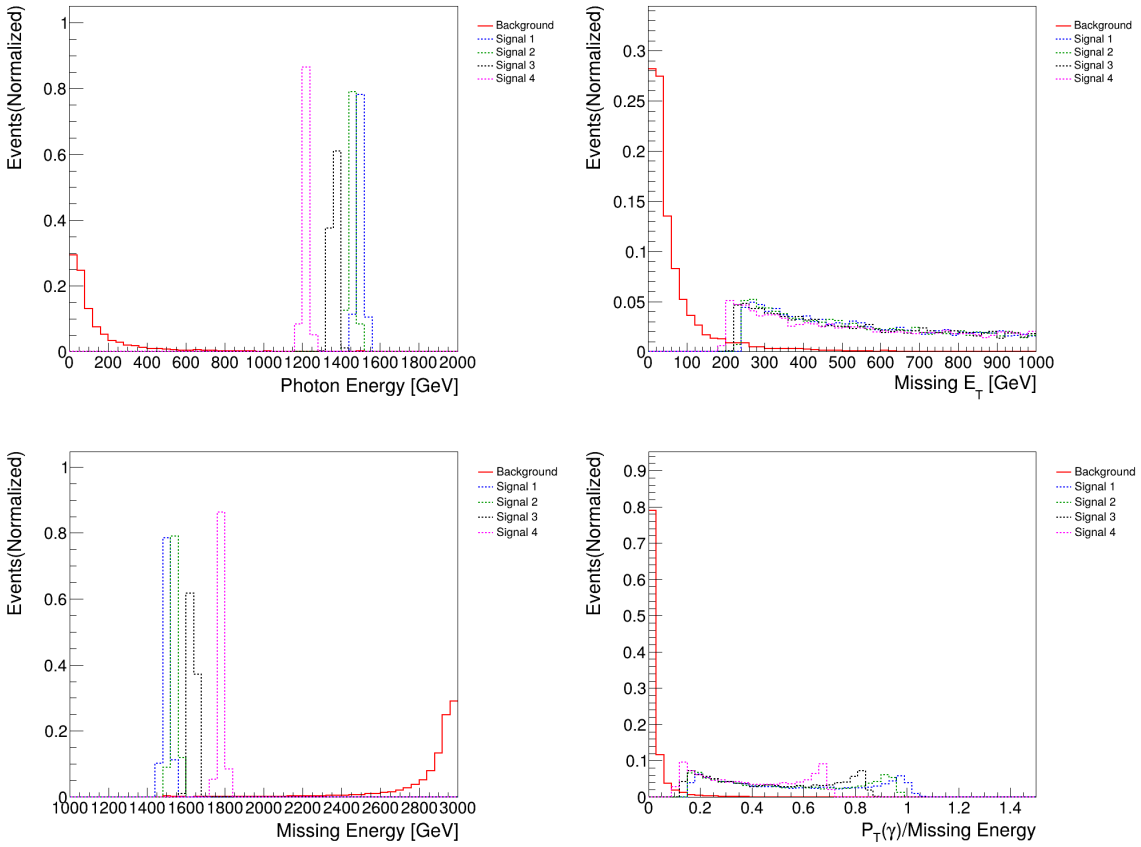

Fig. 3. (color online) In the invisible on-shell mediator decay scenario ($M/m_D = 2.5$) of the $\mathcal{L}_3$ model, representative kinematic distributions include photon energy $E(\gamma)$ (top-left), missing transverse energy $\not{E}_T$ (top-right), missing energy $\not{E}$ (bottom-left), and the ratio of $P_T(\gamma)/\not{E}$ (bottom-right) for signal-1 ($M = 50$ GeV, blue-dotted line), signal-2 ($M = 500$ GeV, green-dotted line), signal-3 ($M = 900$ GeV, black-dotted line), signal-4 ($M = 1300$ GeV, purple-dotted line), and background (red-solid line).

C. Mono-photon signature with off-shell mediator

In regions of parameter space where $M < 2m_D$ for models $\mathcal{L}_3, \mathcal{L}_4, \mathcal{L}_8, \mathcal{L}_9, \mathcal{L}_{10}, \mathcal{L}_{13}, \mathcal{L}_{14}$, visible on-shell mediator decays provide optimal search sensitivity. However, when couplings to DM particles significantly exceed those to muon pairs, mono-photon signatures with off-shell mediators offer complementary probes. We therefore investigate this situation through the off-shell mediator mono-photon channel. DM masses are constrainted to $m_D < 100$ GeV from global fitting results [40]. We consider three mediator-to-DM mass ratios: $M/m_D = \{1.1, 1.5, 1.9\}$ as mentioned in Section II.B. To demonstrate our methodology, we select three representative models: $\mathcal{L}_3$, $\mathcal{L}_9$, and $\mathcal{L}_{13}$, presenting their BPs, kinematic distributions, and event selection criteria before generalizing to other models in Section IV.

We select two representative DM masses, $m_D = 20$

Table 6. Similar to Table 5, but for the $\mathcal{L}_8$ model.

	Cut description	background	signal1	signal2	signal3	signal4
	Cross-section/fb	2980	0.132	0.137	0.152	0.183
	$N(\gamma) > 0$	0.92	0.91	0.91	0.91	0.91
Cut-1	$E(\gamma) > 100\,\text{GeV}$ & $\lvert\eta(\gamma)\rvert < 2.5$	0.35	0.91	0.91	0.91	0.91
	$\not{E}_T > 40\,\text{GeV}$	0.30	0.91	0.91	0.91	0.91
Cut-2	$E(\gamma) > 1200\,\text{GeV}$	7.4×10^{-3}	0.91	0.91	0.91	0.83
Cut-3	$P_T(\gamma)/\not{E} > 0.4$	1.7×10^{-3}	0.50	0.49	0.47	0.34
Cut-4	$M_T > 1600\,\text{GeV}$	1.0×10^{-3}	0.37	0.37	0.36	0.29

and 100 GeV, with three benchmark mediator-to-DM mass ratio: (1) Signal-1: $M/m_D = 1.1$; (2) Signal-2: $M/m_D = 1.5$; and (3) Signal-3: $M/m_D = 1.9$ for each scenario. The benchmark couplings are $g_D = 0.5$, $g_f = 0.1$ for the $\mathcal{L}_3$ model; $M_{D\phi} = 100$ GeV, $g_f = 0.1$ for the $\mathcal{L}_9$ model; and $M_{D\phi} = 10$ GeV, $g_f = 0.1$ for the $\mathcal{L}_{13}$ model. Taking the $\mathcal{L}_3$ model as an example, the signal process is $\mu^+\mu^- \to \chi\bar{\chi}\gamma$ via off-shell mediator ϕ, with irreducible SM background process $\mu^+\mu^- \to \nu\bar{\nu}\gamma$. The corresponding production cross-sections are listed in the second row of Tables 7−12 for the respective models and masses, while kinematic distributions appear in Figs. 4−9.

Owing to off-shell mediator production, significant overlaps may occur between the signal and background distributions in $E(\gamma)$, $\not{E}_T$, and $\not{E}$, compared with the on-shell case in Section III B. However, the $\mathcal{L}_9$ model shows obviously less overlap than the $\mathcal{L}_{13}$ model. Nevertheless, the ratio $P_T(\gamma)/\not{E}$ and M_T distributions (defined in Section III.B) remain effective discriminators except for the $\mathcal{L}_{13}$ model. Applying the same event selections as Section III.B, we summarize the selection efficiencies in Tables 7−12 for the respective models and masses. The distinguishable kinematics for the $\mathcal{L}_9$ model yield higher signal efficiencies after all cuts, while the nearly identical kinematic distributions between the signal and background events for the $\mathcal{L}_{13}$ model pose challenges, resulting in only factor-of-ten signal-background separation. In addition, the signal efficiency increases slightly with M/m_D, but remains largely independent of m_D for values below 100 GeV.

Table 7. Cut-flow table for the off-shell mediator scenario of the $\mathcal{L}_3$ model with $m_D = 20$ GeV and its relevant background with cumulative efficiencies from **Cut-1** to **Cut-4**. The three benchmark points are signal-1 ($M/m_D = 1.1$), signal-2 ($M/m_D = 1.5$), and signal-3 ($M/m_D = 1.9$).

	Cut description	background	signal1	signal2	signal3
	Cross-section/fb	2980	0.42	0.45	0.53
	$N(\gamma) > 0$	0.92	0.91	0.91	0.91
Cut-1	$E(\gamma) > 100\,\text{GeV}$ & $\lvert\eta(\gamma)\rvert < 2.5$	0.35	0.75	0.75	0.78
	$\not{E}_T > 40\,\text{GeV}$	0.30	0.73	0.73	0.76
Cut-2	$E(\gamma) > 1200\,\text{GeV}$	7.4×10^{-3}	0.41	0.43	0.51
Cut-3	$P_T(\gamma)/\not{E} > 0.4$	1.7×10^{-3}	0.24	0.26	0.32
Cut-4	$M_T > 1600\,\text{GeV}$	1.0×10^{-3}	0.19	0.21	0.25

Table 8. Similar to Table 7, but for the $\mathcal{L}_3$ model with $m_D = 100$ GeV.

	Cut description	background	signal1	signal2	signal3
	Cross-section/fb	2980	0.34	0.36	0.45
	$N(\gamma) > 0$	0.92	0.91	0.91	0.91
Cut-1	$E(\gamma) > 100\,\text{GeV}$ & $\lvert\eta(\gamma)\rvert < 2.5$	0.35	0.69	0.70	0.74
	$\not{E}_T > 40\,\text{GeV}$	0.30	0.67	0.68	0.72
Cut-2	$E(\gamma) > 1200\,\text{GeV}$	7.4×10^{-3}	0.28	0.31	0.43
Cut-3	$P_T(\gamma)/\not{E} > 0.4$	1.7×10^{-3}	0.16	0.18	0.26
Cut-4	$M_T > 1600\,\text{GeV}$	1.0×10^{-3}	0.13	0.15	0.21

Table 9. Similar to Table 7, but for the $\mathcal{L}_9$ model with $m_D = 20$ GeV.

	Cut description	background	signal1	signal2	signal3
	Cross-section/fb	2980	0.30	0.42	1.20
	$N(\gamma) > 0$	0.92	0.91	0.91	0.91
Cut-1	$E(\gamma) > 100\,\text{GeV}$ & $\lvert\eta(\gamma)\rvert < 2.5$	0.35	0.91	0.91	0.91
	$\not{E}_T > 40\,\text{GeV}$	0.30	0.91	0.91	0.91
Cut-2	$E(\gamma) > 1200\,\text{GeV}$	7.4×10^{-3}	0.91	0.91	0.91
Cut-3	$P_T(\gamma)/\not{E} > 0.4$	1.7×10^{-3}	0.57	0.58	0.58
Cut-4	$M_T > 1600\,\text{GeV}$	1.0×10^{-3}	0.45	0.46	0.46

Table 10. Similar to Table 7, but for the $\mathcal{L}_9$ model with $m_D = 100$ GeV.

	Cut description	background	signal1	signal2	signal3
	Cross-section/fb	2980	1.3×10^{-2}	1.8×10^{-2}	4.9×10^{-2}
	$N(\gamma) > 0$	0.92	0.91	0.91	0.91
Cut-1	$E(\gamma) > 100\,\text{GeV}$ & $\lvert\eta(\gamma)\rvert < 2.5$	0.35	0.90	0.90	0.91
	$\not{E}_T > 40\,\text{GeV}$	0.30	0.90	0.90	0.91
Cut-2	$E(\gamma) > 1200\,\text{GeV}$	7.4×10^{-3}	0.85	0.87	0.90
Cut-3	$P_T(\gamma)/\not{E} > 0.4$	1.7×10^{-3}	0.53	0.53	0.56
Cut-4	$M_T > 1600\,\text{GeV}$	1.0×10^{-3}	0.42	0.43	0.44

Table 11. Similar to Table 7, but for the $\mathcal{L}_{13}$ model with $m_D = 20$ GeV.

	Cut description	background	signal1	signal2	signal3
	Cross-section/fb	2980	518	533	521
	$N(\gamma) > 0$	0.92	0.91	0.91	0.91
Cut-1	$E(\gamma) > 100\,\text{GeV}$ & $\lvert\eta(\gamma)\rvert < 2.5$	0.35	0.54	0.54	0.53
	$\not{E}_T > 40\,\text{GeV}$	0.30	0.51	0.50	0.49
Cut-2	$E(\gamma) > 1200\,\text{GeV}$	7.4×10^{-3}	3.0×10^{-2}	2.8×10^{-2}	3.2×10^{-2}
Cut-3	$P_T(\gamma)/\not{E} > 0.4$	1.7×10^{-3}	1.5×10^{-2}	1.6×10^{-2}	1.8×10^{-2}
Cut-4	$M_T > 1600\,\text{GeV}$	1.0×10^{-3}	1.3×10^{-2}	1.3×10^{-2}	1.6×10^{-2}

Table 12. Similar to Table 7, but for the $\mathcal{L}_{13}$ model with $m_D = 100$ GeV.

	Cut description	background	signal1	signal2	signal3
	Cross-section/fb	2980	0.83	0.84	0.84
	$N(\gamma) > 0$	0.92	0.91	0.91	0.92
Cut-1	$E(\gamma) > 100\,\text{GeV}$ & $\lvert\eta(\gamma)\rvert < 2.5$	0.35	0.53	0.53	0.52
	$\not{E}_T > 40\,\text{GeV}$	0.30	0.48	0.49	0.49
Cut-2	$E(\gamma) > 1200\,\text{GeV}$	7.4×10^{-3}	2.6×10^{-2}	2.7×10^{-2}	3.2×10^{-2}
Cut-3	$P_T(\gamma)/\not{E} > 0.4$	1.7×10^{-3}	1.4×10^{-2}	1.4×10^{-2}	1.8×10^{-2}
Cut-4	$M_T > 1600\,\text{GeV}$	1.0×10^{-3}	1.3×10^{-2}	1.2×10^{-2}	1.5×10^{-2}

D. Vector boson fusion production: visible and invisible mediator decays

As the vector boson fusion (VBF) production at the TeV muon collider becomes more dominant, we further extend the search strategies to VBF production at the 3 TeV muon collider, with the hard process defined as $\mu^+\mu^- \to \nu_\mu\bar{\nu}_\mu\mu^+\mu^-\text{MED}$. The mediator, MED, subsequently decays into either a muon pair ($\text{MED} \to \mu^+\mu^-$, visible decay) or a DM pair ($\text{MED} \to \text{DM}+\text{DM}$, invis-

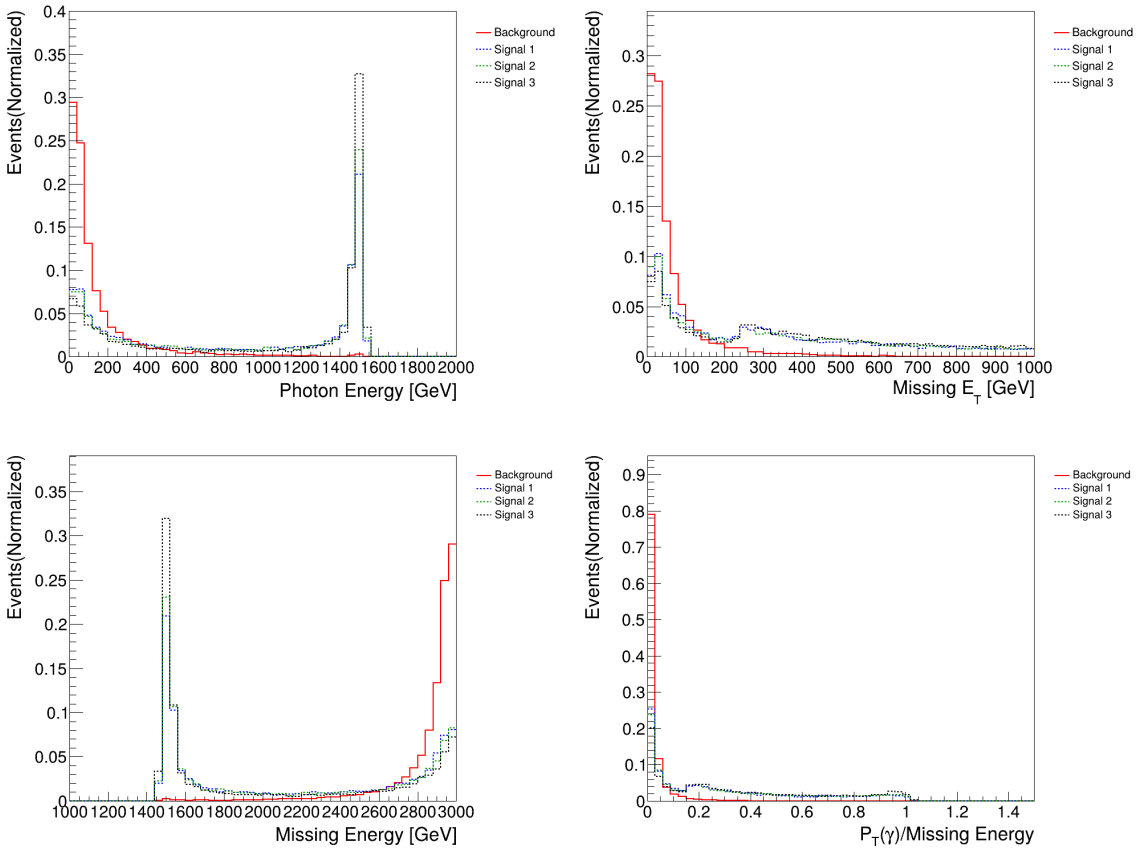

Fig. 4. (color online) Off-shell mediator scenario of the $\mathcal{L}_3$ model with $m_D = 20$ GeV. Representative kinematic distributions include photon energy $E(\gamma)$ (top-left), missing transverse energy $\not{E}_T$ (top-right), missing energy $\not{E}$ (bottom-left), and the ratio of $P_T(\gamma)/\not{E}$ (bottom-right) for signal-1 ($M/m_D = 1.1$, blue-dotted line), signal-2 ($M/m_D = 1.5$, green-dotted line), signal-3 ($M/m_D = 1.9$, black-dotted line), and background (red-solid line).

ible decay). This process is driven by the weak interaction of the initial-state muon pair, with the on-shell mediator emitted from one of the muon legs. The fixed mass ratio $M/m_D = 2.5$ is imposed to ensure the kinematic accessibility of both decay channels. The coupling parameter ratios follow Table 13 to guarantee the branching ratio of either $\mathcal{B}(\text{MED} \to \mu^+\mu^-) > 99\%$ or $\mathcal{B}(\text{MED} \to \text{DM+DM}) > 99\%$.

For the visible decay channel: $\text{MED} \to \mu^+\mu^-$, the full signal process is $\mu^+\mu^- \to \nu_\mu\bar{\nu}_\mu\mu^+\mu^-\text{MED}$, where $\text{MED} \to \mu^+\mu^-$. The major irreducible background is $\mu^+\mu^- \to \nu_l\bar{\nu}_l\mu^+\mu^-\mu^+\mu^-$. For the $\mathcal{L}_3$ model, the benchmark coupling parameters are set to $g_f = 0.01$ and $g_D = 0.08$, corresponding to a coupling constant ratio of $g_D/g_f = 1/8$. For the $\mathcal{L}_8$ model, the benchmark coupling parameters are set to $g_f = 0.01$ and $g_D = 0.09$, with the corresponding coupling constant ratio of $g_D/g_f = 1/9$.

Some relevant kinematic distributions of signal and background processes are shown in Fig. 10. Based on the above kinematic distributions, we optimized the event selection criteria for the multimuon final state with missing energy as follows:

- Cut-1 (basic cuts): $N_{\mu^+} \geq 2$, $N_{\mu^-} \geq 2$, $\not{E}_T > 40$ GeV, $p_T(\mu) > 20$ GeV, and $|\eta(\mu)| < 2.5$;
- Cut-2: $2.2 < \Delta R(\mu_1\mu_2) < 3.3$;
- Cut-3: $p_T(\mu_1) \geq 130$ GeV, and $|\eta(\mu_1)| < 0.75$;
- Cut-4: $\not{E}_T > 350$ GeV;
- Cut-5: $|M_{\mu\mu}^{\text{best}} - M| < 0.1M$.

where the ordering of the subscripts μ_1 and μ_2 is determined by their p_T values, and $M_{\mu\mu}^{\text{best}}$ denotes the dimuon pair with invariant mass closest to the mediator mass, selected from all possible dimuon pairs formed by the four muons.

For the invisible decay channel: $\text{MED} \to \text{DM} + \text{DM}$, the full signal process is $\mu^+\mu^- \to \nu_\mu\bar{\nu}_\mu\mu^+\mu^-\text{MED}$, where $\text{MED} \to \text{DM} + \text{DM}$, with missing energy from both neutrino and DM particles. The major background comes from $\mu^+\mu^- \to \nu_l\bar{\nu}_l\mu^+\mu^-$. For the $\mathcal{L}_3$ model, the benchmark coupling parameters are set to $g_f = 0.15$ and $g_D = 0.01$, corresponding to a coupling constant ratio of $g_D/g_f = 15$.

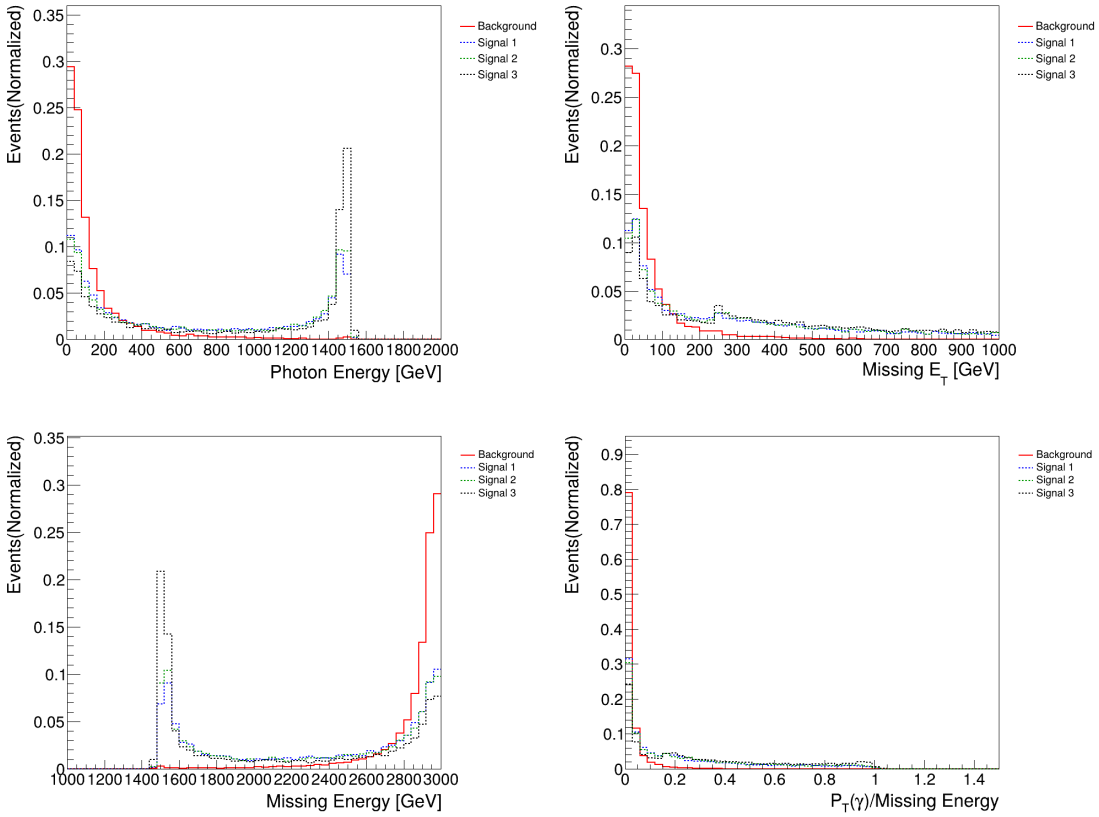

Fig. 5. (color online) Similar to Fig. 4, but for the $\mathcal{L}_3$ model with $m_D = 100$ GeV.

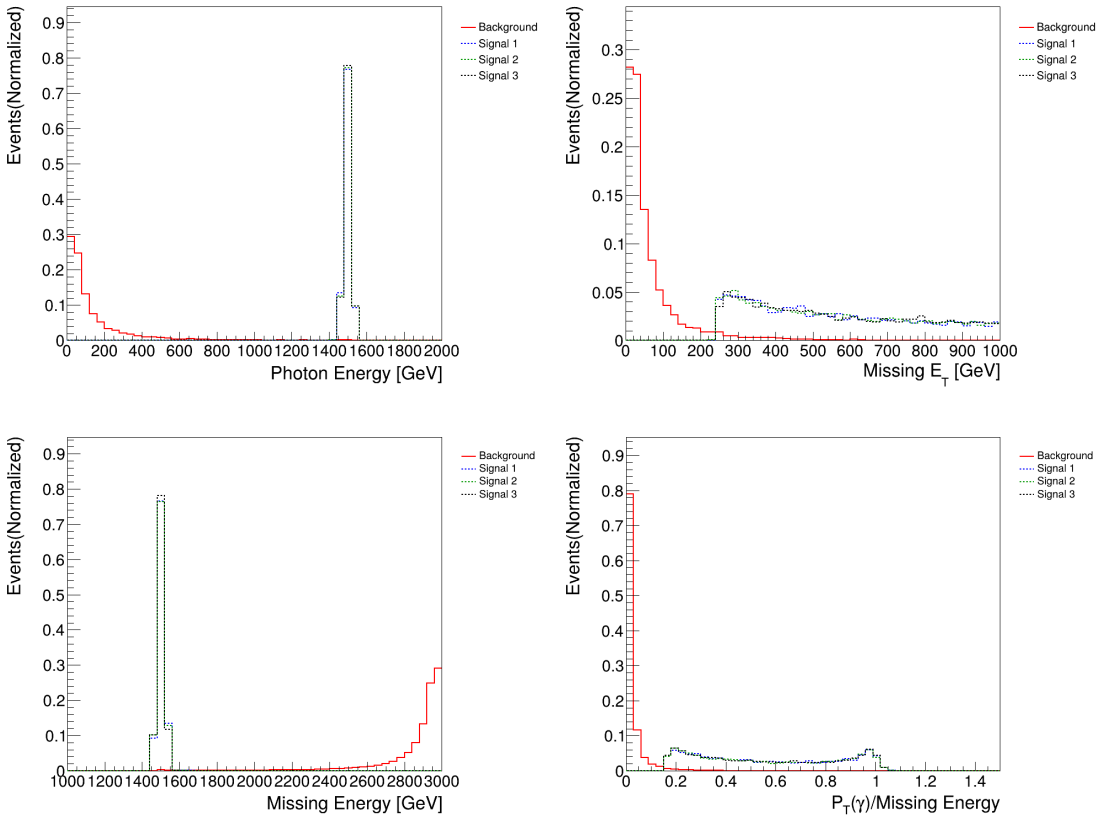

Fig. 6. (color online) Similar to Fig. 4, but for the $\mathcal{L}_9$ model with $m_D = 20$ GeV.

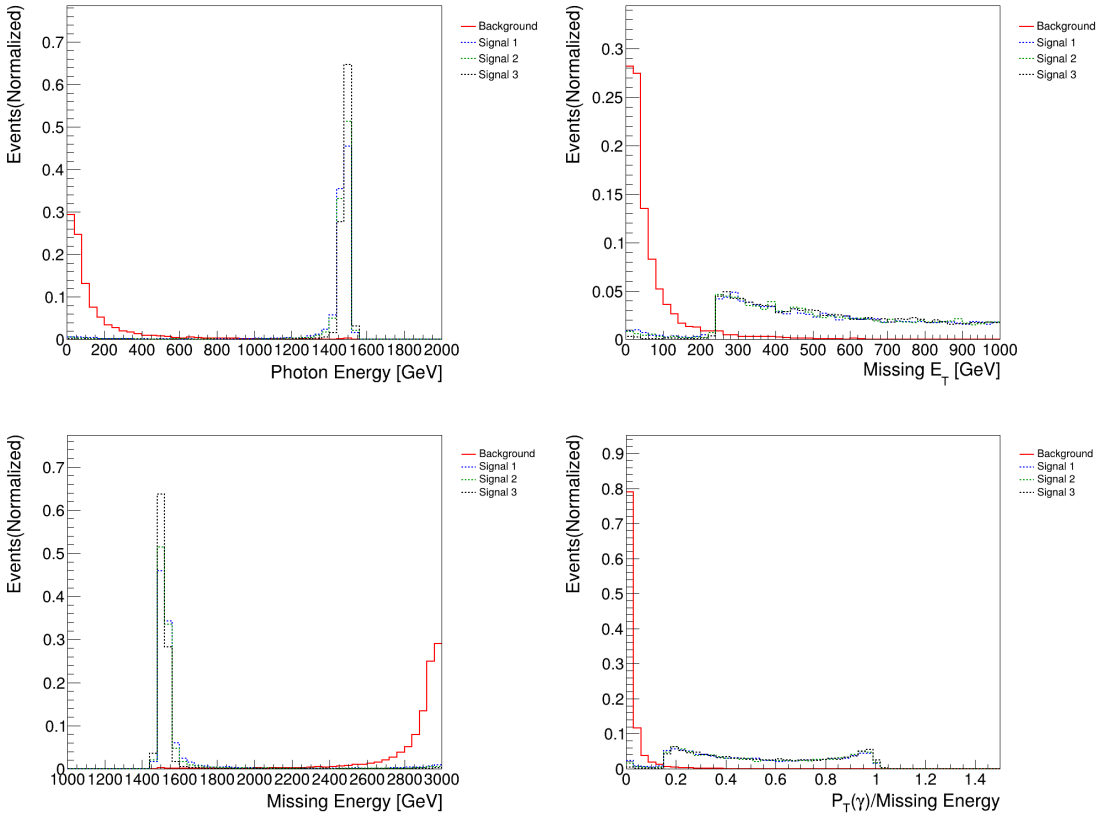

Fig. 7. (color online) Similar to Fig. 4, but for the $\mathcal{L}_9$ model with $m_D = 100$ GeV.

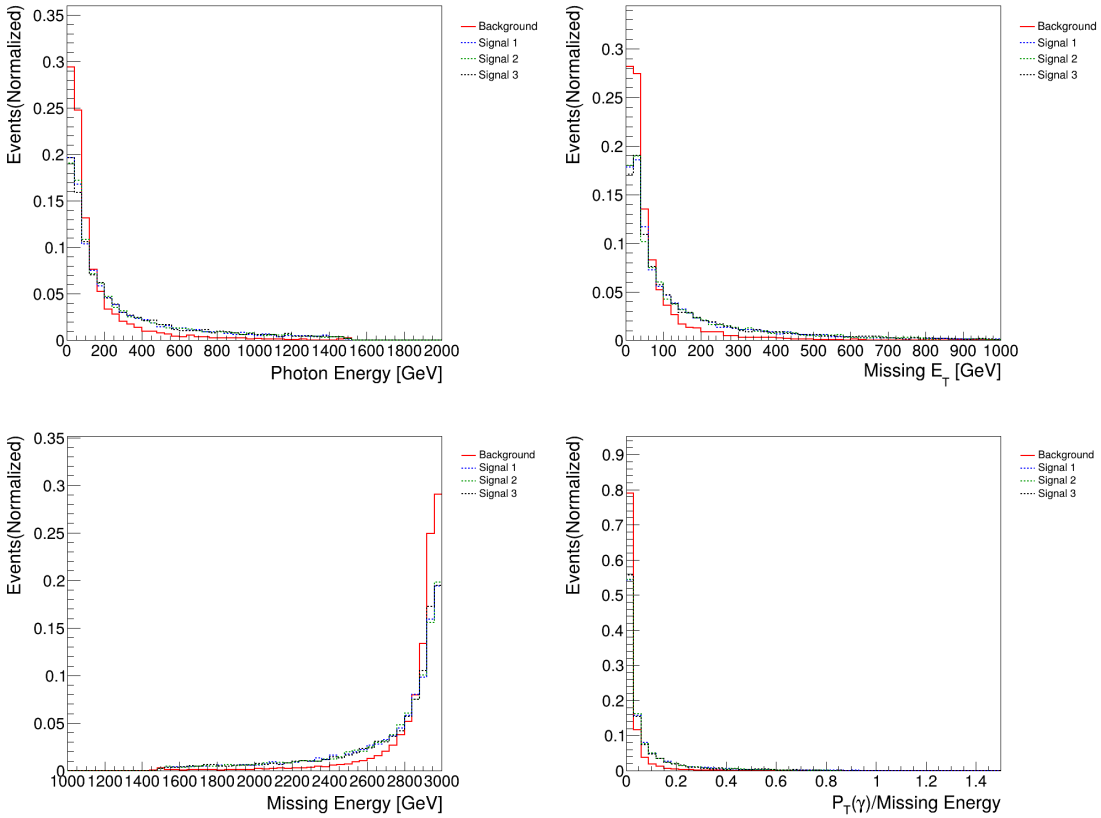

Fig. 8. (color online) Similar to Fig. 4, but for the $\mathcal{L}_{13}$ model with $m_D = 20$ GeV.

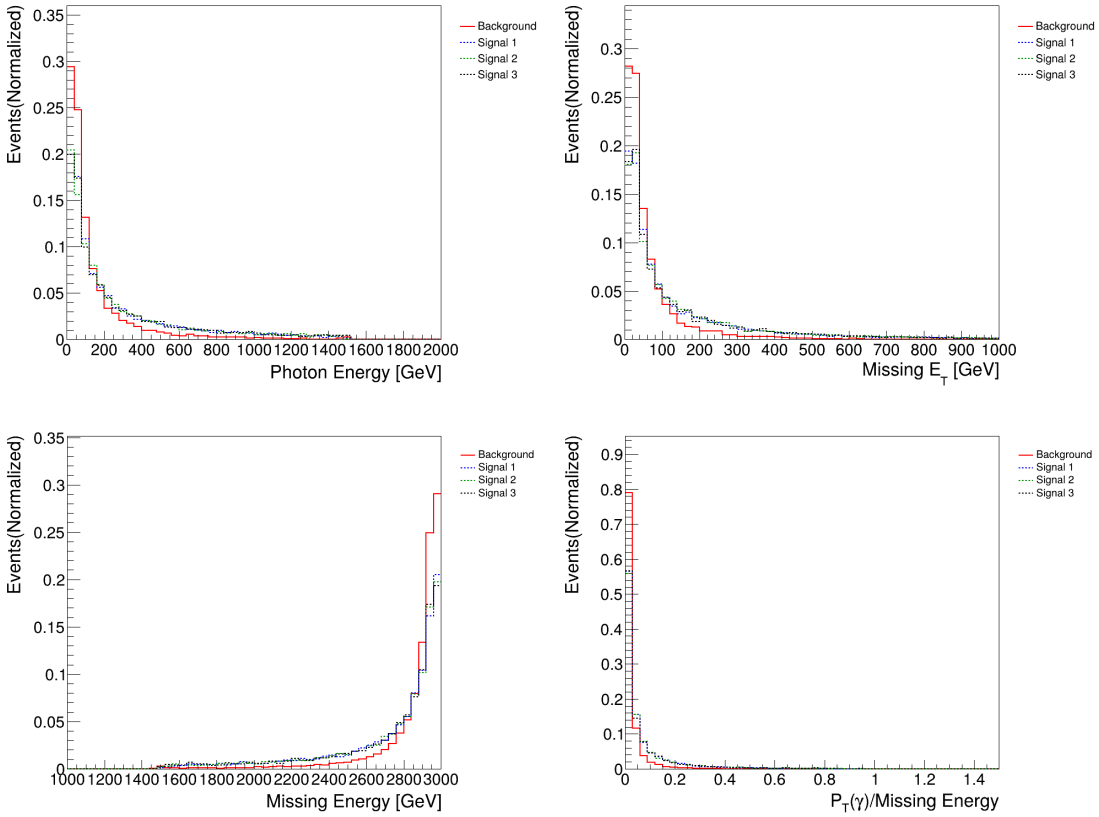

Fig. 9. (color online) Similar to Fig. 4, but for the $\mathcal{L}_{13}$ model with $m_D = 100$ GeV.

Table 13. Cut-flow table for visible on-shell mediator decay scenario ($M/m_D = 2.5$) of the $\mathcal{L}_3$ model in the VBF process and its relevant background with cumulative efficiencies from **Cut-1** to **Cut-5**. The four BPs are signal-1 ($M = 50$ GeV), signal-2 ($M = 500$ GeV), signal-3 ($M = 900$ GeV), and signal-4 ($M = 1300$ GeV).

	Cut description	background	signal1	signal2	signal3	signal4
	Cross-section/fb	0.428	2.061	2.078	1.473	0.899
Cut-1	$N_{\mu^+} \geq 2$ and $N_{\mu^-} \geq 2$, $p_T(\mu) > 20$ GeV, $\lvert\eta(\mu)\rvert < 2.5$, $\not{E}_T > 40$ GeV	0.65	0.79	0.84	0.83	0.82
Cut-2	$2.2 < \Delta R(\mu_1,\mu_2) < 3.3$	0.15	0.48	0.50	0.49	0.60
Cut-3	$p_T(\mu_1) \geq 130$ GeV, $\lvert\eta(\mu_1)\rvert < 0.75$	0.05	0.38	0.42	0.41	0.49
Cut-4	$\not{E}_T > 350$ GeV	0.01	0.23	0.26	0.23	0.25
Cut-5	$\lvert M_{\mu\mu}^{\text{best}} - M\rvert < 0.1M$	6.0×10^{-4}	0.22	/	/	/
		6.0×10^{-3}	/	0.25	/	/
		5.4×10^{-3}	/	/	0.22	/
		6.5×10^{-3}	/	/	/	0.24

For the $\mathcal{L}_8$ model, the benchmark coupling parameters are set to $g_f = 0.12$ and $g_D = 0.01$, with the corresponding coupling constant ratio of $g_D/g_f = 12$.

Figure 11 shows the relevant kinematic distributions for signal and background processes. The event selection criteria are designed to enhance the discrimination between signal and background processes as follows:

- Cut-1 (basic cuts): $N_{\mu^+} \geq 1$, $N_{\mu^-} \geq 1$, $p_T(\mu) > 20$ GeV, $\lvert\eta(\mu)\rvert < 2.5$, and $\not{E}_T > 40$ GeV;
- Cut-2: $E(\mu_1) \geq 350$ GeV, and $\lvert\eta(\mu_1)\rvert < 0.8$;
- Cut-3: $\not{E}_T > 250$ GeV;
- Cut-4: $p_T(\mu_1)/\not{E} > 0.12$.

Finally, we show the cut-flow in Tables 13, 14 and Tables 15, 16 for various signal BPs of $\mathcal{L}_3$ and $\mathcal{L}_8$ models as well as the background in the VBF process under

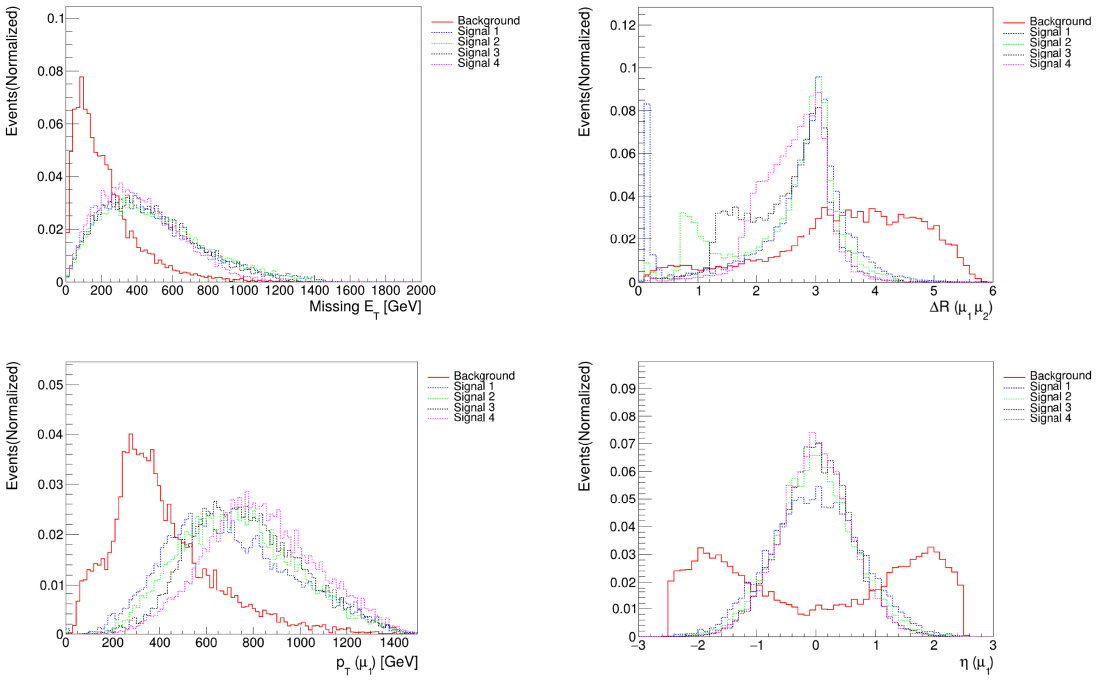

Fig. 10. (color online) Visible on-shell mediator decay scenario ($M/m_D = 2.5$) of the $\mathcal{L}_3$ model in the VBF process. Representative kinematic distributions include missing transverse energy $\not{E}_T$ (top-left), angular separation $\Delta R(\mu_1\mu_2)$ (top-right), transverse momentum of leading muon $p_T(\mu_1)$ (bottom-left), and pseudorapidity of leading muon $|\eta(\mu_1)|$ (bottom-right) for signal-1 ($M = 50$ GeV, blue-dotted line), signal-2 ($M = 500$ GeV, green-dotted line), signal-3 ($M = 900$ GeV, black-dotted line), signal-4 ($M = 1300$ GeV, purple-dotted line), and background (red-solid line).

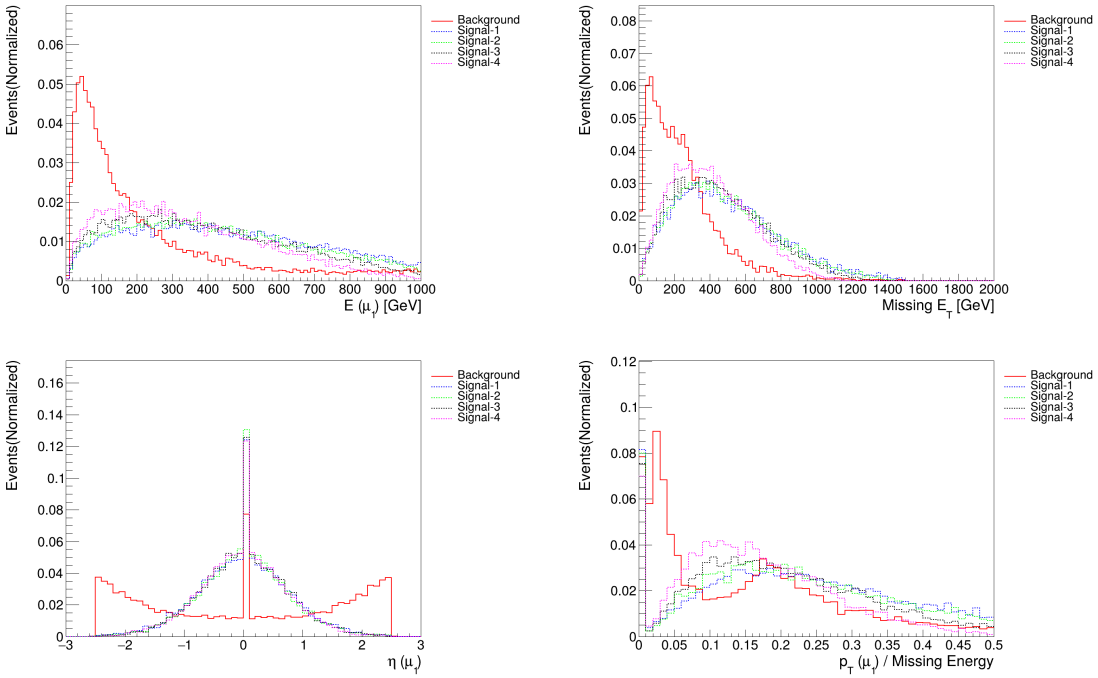

Fig. 11. (color online) Invisible on-shell mediator decay scenario ($M/m_D = 2.5$) of the $\mathcal{L}_3$ model in the VBF process. Representative kinematic distributions include leading muon energy $E(\mu_1)$ (top-left), missing transverse energy $\not{E}_T$ (top-right), pseudorapidity of leading muon $|\eta(\mu_1)|$ (bottom-left), and transverse momentum ratio of leading muon to missing energy (bottom-right) for signal-1 ($M = 50$ GeV, blue-dotted line), signal-2 ($M = 500$ GeV, green-dotted line), signal-3 ($M = 900$ GeV, black-dotted line), signal-4 ($M = 1300$ GeV, purple-dotted line), and background (red-solid line).

Table 14. Similar to Table 13, but for the $\mathcal{L}_8$ model.

	Cut description	background	signal1	signal2	signal3	signal4
	Cross-section/fb	0.428	891.3	20.3	7.823	3.748
Cut-1	$N_{\mu^+} \geq 2$ and $N_{\mu^-} \geq 2$, $p_T(\mu) > 20$ GeV, $\lvert\eta(\mu)\rvert < 2.5$, $\not{E}_T > 40$ GeV	0.65	0.80	0.83	0.83	0.83
Cut-2	$2.2 < \Delta R(\mu_1, \mu_2) < 3.3$	0.15	0.53	0.51	0.49	0.59
Cut-3	$p_T(\mu_1) \geq 130$ GeV, $\lvert\eta(\mu_1)\rvert < 0.75$	0.05	0.44	0.45	0.41	0.46
Cut-4	$\not{E}_T > 350$ GeV	0.01	0.28	0.28	0.23	0.22
Cut-5	$\lvert M_{\mu\mu}^{\text{best}} - M\rvert < 0.1M$	6.0×10^{-4}	0.27	/	/	/
		6.0×10^{-3}	/	0.27	/	/
		5.4×10^{-3}	/	/	0.22	/
		6.5×10^{-3}	/	/	/	0.20

Table 15. Cut-flow table for invisible on-shell mediator decay scenario ($M/m_D = 2.5$) of the $\mathcal{L}_3$ model in the VBF process and its relevant background with cumulative efficiencies from **Cut-1** to **Cut-4**. The four BPs are signal-1 ($M = 50$ GeV), signal-2 ($M = 500$ GeV), signal-3 ($M = 900$ GeV), and signal-4 ($M = 1300$ GeV).

	Cut description	background	signal1	signal2	signal3	signal4
	Cross-section/fb	165	4.20×10^{-2}	3.36×10^{-2}	2.36×10^{-2}	1.46×10^{-2}
Cut-1	$N_{\mu^+} \geq 1$ and $N_{\mu^-} \geq 1$, $p_T(\mu) > 20$ GeV, $\lvert\eta(\mu)\rvert < 2.5$ $\not{E}_T > 40$ GeV	0.79	0.90	0.90	0.90	0.90
Cut-2	$E(\mu_1) \geq 350$ GeV, $\lvert\eta(\mu_1)\rvert < 0.8$	0.05	0.59	0.59	0.56	0.52
Cut-3	$\not{E}_T > 350$ GeV	0.04	0.46	0.46	0.44	0.40
Cut-4	$P_T(\mu_1)/\not{E} > 0.12$	0.03	0.45	0.45	0.43	0.39

Table 16. Similar to Table 15, but for the $\mathcal{L}_8$ model.

	Cut description	background	signal1	signal2	signal3	signal4
	Cross-section/fb	165	19.28	0.26	9.99×10^{-2}	4.83×10^{-2}
Cut-1	$N_{\mu^+} \geq 1$ and $N_{\mu^-} \geq 1$, $p_T(\mu) > 20$ GeV, $\lvert\eta(\mu)\rvert < 2.5$ $\not{E}_T > 40$ GeV	0.79	0.91	0.91	0.90	0.91
Cut-2	$E(\mu_1) \geq 350$ GeV, $\lvert\eta(\mu_1)\rvert < 0.8$	0.05	0.66	0.64	0.59	0.55
Cut-3	$\not{E}_T > 350$ GeV	0.04	0.58	0.53	0.46	0.39
Cut-4	$P_T(\mu_1)/\not{E} > 0.12$	0.03	0.57	0.52	0.45	0.38

the visible and invisible on-shell mediator decay scenarios ($M/m_D = 2.5$), respectively.

IV. RESULTS AND DISCUSSIONS

After establishing the four search strategies in Section III, we determined the efficiencies ($\epsilon_{s,b}$) for both signal and background events. Two specific scenarios required adjustments to the selection criteria. First, for mediator masses near 1500 GeV, the initial requirement of $E(\gamma) > 1200$ GeV in Cut-2 for the search of invisible on-shell mediator decays proved overly restrictive; we therefore relaxed it to $E(\gamma) > 1000$ GeV. Similarly, for the mediator mass close to 20 GeV in the analysis of visible on-shell mediator decays, the pseudorapidity requirements in Cut-2, Cut-3, and the original $p_T(\mu^\pm) > 150$ GeV in Cut-3 were found to be overly stringent. Therefore, we relaxed them to $p_T(\mu^\pm) > 50$ GeV, $\lvert\eta(\gamma)\rvert < 2.2$, and $\lvert\eta(\mu^\pm)\rvert < 2.2$, respectively. Signal and background production cross-sections ($\sigma_{s,b}$) were computed using `MadGraph5_aMC@NLO`. In addition, we adopted an optimistic integrated luminosity of $L = 4400$ fb^{-1} [89, 90]. The expected numbers of signal and background events are given by $N_{s,b} = \sigma_{s,b} \times \epsilon_{s,b} \times L$.

After obtaining the signal and background event counts, the signal significance is calculated as [91, 92]

$$Z = \sqrt{2 \cdot [(N_s + N_b) \cdot \ln(1 + \frac{N_s}{N_b}) - N_s]}. \tag{3}$$

To account for systematic uncertainties in the background, this formula is modified to [92, 93]

$$Z = \sqrt{2 \cdot \left[(N_s + N_b) \cdot \ln \left[\frac{(N_s + N_b)(N_b + \sigma_b^2)}{N_b^2 + (N_s + N_b)\sigma_b^2} \right] - \frac{N_s^2}{\sigma_b^2} \cdot \ln \left(1 + \frac{N_b \sigma_b^2}{N_s^2 + N_b \sigma_b^2} \right) \right]}. \tag{4}$$

In this work, we adopted a conservative estimate for the systematic uncertainty, setting $\sigma_b = 0.05 N_b$, which corresponds to a flat 5% of the total background event. This flat 5% systematic uncertainty is determined by referring to the typical estimation range of systematic uncertainties in muon collider studies. We used a significance threshold of $Z = 1.96$, corresponding to a 95% confidence level, to project the future exclusion limits for $\mathcal{L}_3$, $\mathcal{L}_4$, $\mathcal{L}_8$, $\mathcal{L}_9$, $\mathcal{L}_{10}$, $\mathcal{L}_{13}$, and $\mathcal{L}_{14}$ at a 3 TeV muon collider.

For visible on-shell mediator decays, we imposed the condition $\mathcal{B}(\text{MED} \to \mu^+\mu^-) > 99\%$ to determine the coupling parameter ratios, which in turn fixed g_D/g_f for the $\mathcal{L}_3$, $\mathcal{L}_4$, and $\mathcal{L}_8$ models and $M_{D\phi}/g_f$ for the $\mathcal{L}_9$, $\mathcal{L}_{10}$, $\mathcal{L}_{13}$, and $\mathcal{L}_{14}$ models. These ratios are listed in the third column of Table 17. We find that the coupling parameter ratios for four models ($\mathcal{L}_9$, $\mathcal{L}_{10}$, $\mathcal{L}_{13}$, and $\mathcal{L}_{14}$) span a range of values rather than taking a single fixed one. This behavior occurs because of the one-dimensional coupling $M_{D\phi}$, which is closely related to the mediator mass for the mediator branching ratio calculations. Specifically, the ratio $M_{D\phi}/g_f$ required to satisfy $\mathcal{B}(\text{MED} \to \mu^+\mu^-) > 99\%$ increased monotonically with the mediator mass. Relaxing the branching ratio condition to values below 99% would lead to a decrease in both the g_D/g_f and $M_{D\phi}/g_f$ ratios.

Using a mass ratio of $M/m_D = 2.5$ (ensuring $M > 2m_D$) and benchmark mediator masses M from 20 GeV to 1500 GeV, we derived the projected exclusion limits at significance $Z = 1.96$. Our analysis shows that once the condition $M > 2m_D$ is met, the results depended only moderately on the specific value of the M/m_D ratio. The solid and dashed lines in Fig. 12 show these projected exclusion limits without and with a flat 5% systematic uncertainty, respectively.

The exclusion lines of all seven models exhibited an overall increasing trend with the increase of the mediator mass M; however, a distinct peak emerged at $M = 100$ GeV for all models. Specifically, the exclusion lines corresponding to the $\mathcal{L}_3$, $\mathcal{L}_4$, and $\mathcal{L}_8$ models show a monotonically decreasing behavior within the mass interval of 20–50 GeV, while those associated with the $\mathcal{L}_9$, $\mathcal{L}_{10}$, $\mathcal{L}_{13}$, and $\mathcal{L}_{14}$ models increased monotonically as M increases.

The origin of this characteristic behavior is as follows. For the mediator with $M = 20$ GeV, relaxed kinematic selection criteria are adopted in this work, which resulted in the background detection efficiency being enhanced to twice its nominal value. To satisfy the statistical significance threshold of $Z = 1.96$, the required production cross-section for $M = 20$ GeV is correspondingly increased. Under the standard selection criteria, the background detection efficiency at $M = 100$ GeV is significantly higher than that at adjacent mass points. This phenomenon is mainly attributed to the fact that the rest mass of the Z boson is approximately 91 GeV, a large number of Z bosons are resonantly produced in this energy regime, and the energy spectrum broadening effect in experiments extends this resonance peak to the vicinity of 100 GeV. The Z bosons are abundantly produced and decay near this mass interval, generating a considerable number of detectable final-state particles, which in turn leads to a significant enhancement of the background detection efficiency within the 100 GeV mass window. This is the core reason why a distinct peak appears at $M = 100$ GeV for all models.

To assess the consistency of our results with a GCE interpretation, we overlay the GCE-favored parameter regions, subject to the relevant constraints identified in Ref. [40], onto Figs. 12 and 13. These regions are shown as colored bands corresponding to different mediator-to-DM mass ratios M/m_D. For the $\mathcal{L}_3$, $\mathcal{L}_4$, and $\mathcal{L}_8$ models, we

Table 17. Ratio of coupling parameters g_D/g_f (for $\mathcal{L}_3$, $\mathcal{L}_4$, $\mathcal{L}_8$) and $M_{D\phi}$ (TeV)$/g_f$ (for $\mathcal{L}_9$, $\mathcal{L}_{10}$, $\mathcal{L}_{13}$, $\mathcal{L}_{14}$) used in this analysis for visible on-shell mediator decays with the condition $\mathcal{B}(\text{MED} \to \mu^+\mu^-) > 99\%$ and invisible on-shell mediator decays with the condition $\mathcal{B}(\text{MED} \to \text{DM} + \text{DM}) > 99\%$, respectively.

Models	Coupling parameter	Visible on-shell mediator decays	Invisible on-shell mediator decays
$\mathcal{L}_3$	g_D/g_f	1/8	15
$\mathcal{L}_4$	g_D/g_f	1/8	15
$\mathcal{L}_8$	g_D/g_f	1/9	12
$\mathcal{L}_9$	$M_{D\phi}$ (TeV)$/g_f$	3.66×10^{-3} – 2.75×10^{-1}	0.91–27.3
$\mathcal{L}_{10}$	$M_{D\phi}$ (TeV)$/g_f$	3.66×10^{-3} – 2.75×10^{-1}	0.91–27.3
$\mathcal{L}_{13}$	$M_{D\phi}$ (TeV)$/g_f$	1.43×10^{-3} – 1.07×10^{-1}	0.356–10.68
$\mathcal{L}_{14}$	$M_{D\phi}$ (TeV)$/g_f$	1.43×10^{-3} – 1.07×10^{-1}	0.356–10.68

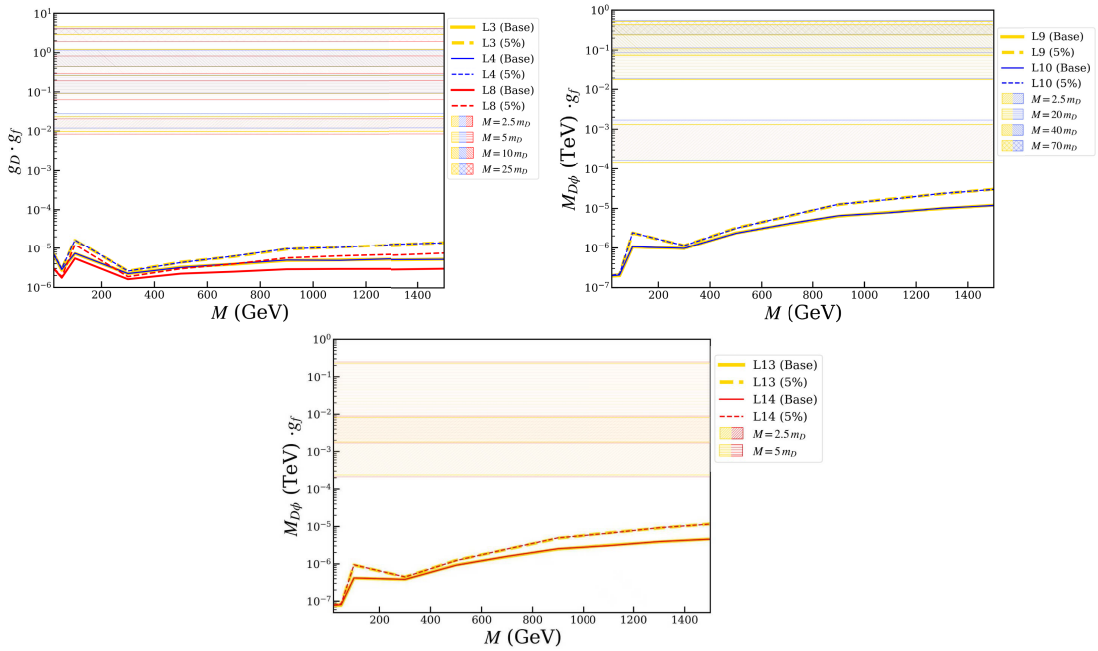

Fig. 12. (color online) Projected exclusion limits at 95% confidence level on the parameter space for visible on-shell mediator decays in seven models. The solid and dashed lines correspond to the cases without and with a flat 5% background systematic uncertainty, respectively. The condition $\mathcal{B}(\text{MED} \to \mu^+\mu^-) > 99\%$ is imposed to determine the ratio of coupling parameters g_D/g_f (for $\mathcal{L}_3$, $\mathcal{L}_4$, $\mathcal{L}_8$) and $M_{D\phi}$ (TeV)$/g_f$ (for $\mathcal{L}_9$, $\mathcal{L}_{10}$, $\mathcal{L}_{13}$, $\mathcal{L}_{14}$), as shown in Table 17. Colored bands denote the GCE-favored parameter regions consistent with Ref. [40], where distinct colors correspond to individual models and various patterns within the bands distinguish the mediator-to-DM mass ratios M/m_D (see the main text for details).

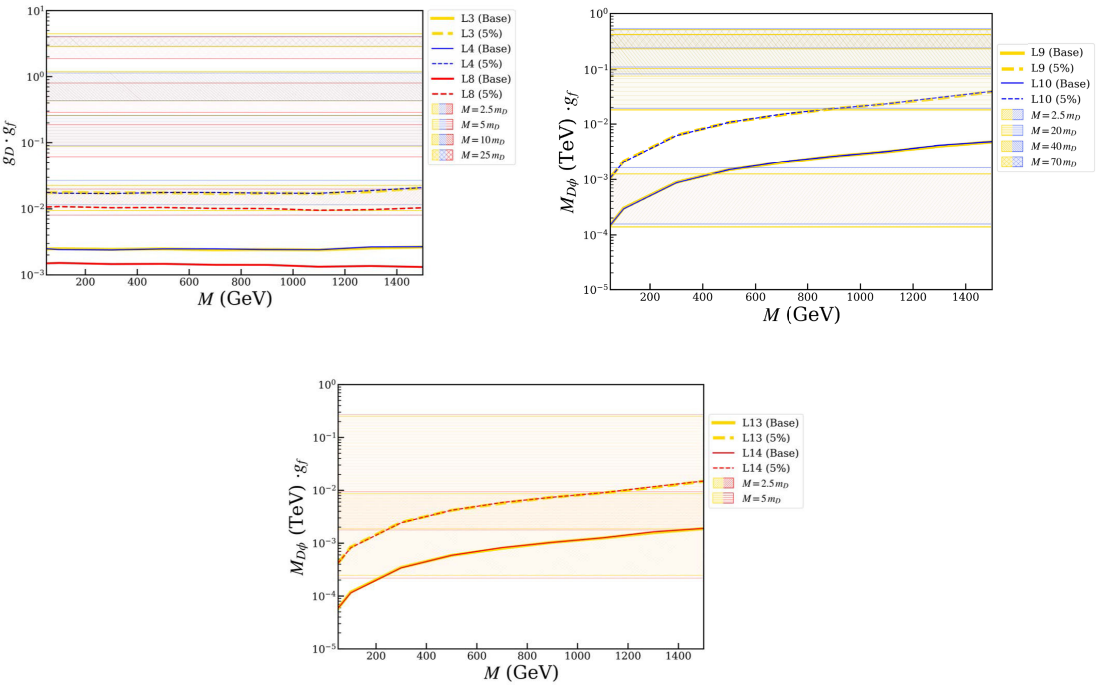

Fig. 13. (color online) Similar to Fig. 12, but for invisible on-shell mediator decays in seven models and applying the condition $\mathcal{B}(\text{MED} \to \text{DM} + \text{DM}) > 99\%$ to determine the ratio of coupling parameters.

used $M/m_D = \{2.5, 5, 10, 25\}$; for the $\mathcal{L}_9$ and $\mathcal{L}_{10}$ models, we used $M/m_D = \{2.5, 20, 40, 70\}$. Although the $\mathcal{L}_{13}$ and $\mathcal{L}_{14}$ models are studied with $M/m_D = \{2.5, 5, 7.5, 10\}$, only the bands for $\{2.5, 5\}$ are displayed, as they fully encompass the parameter space covered by the higher ratios, making the latter redundant for visualization. Remark-

ably, in the visible decay case, all projected exclusion lines lie consistently below the GCE-favored bands across the investigated mass range, indicating a robust probe of the GCE explanation.

To quantify the dependence of our final exclusion limits on the ratio of M/m_D, we performed a supplementary comparative analysis with different M/m_D values. In the baseline analysis of this work, we fixed $M/m_D = 2.5$ and extended the study to two alternative values $M/m_D = 5$ and $M/m_D = 10$. For the visible on-shell mediator decay channel, in the $\mathcal{L}_3$ model with the fixed baseline coupling ratio $g_D/g_f = 1/8$, the mediator decay branching ratio $\mathcal{B}(\text{MED} \to \mu^+\mu^-)$ is lower than the 99% threshold set in the previous assumption, and slightly decreased with the increase of M/m_D: it drops to 98.6% when $M/m_D = 5$, and further decreases to 98.5% when $M/m_D = 10$. In the $\mathcal{L}_8$ model with the fixed baseline coupling ratio $g_D/g_f = 1/9$, the branching ratio is also lower than the 99% threshold, showing a slight fluctuation: it is 98.79% when $M/m_D = 5$, and slightly decreased to 98.78% when $M/m_D = 10$. On the other hand, the variation of M/m_D has negligible effects on the signal detection efficiency. Taking the representative $\mathcal{L}_3$ and $\mathcal{L}_8$ models as examples, for the $\mathcal{L}_3$ model, the relative deviations of the exclusion limits for $M/m_D = 5$ and $M/m_D = 10$ with respect to the baseline $M/m_D = 2.5$ are approximately 11% and 19%, respectively; for the $\mathcal{L}_8$ model, the relative deviations are approximately 9% and 25%, respectively.

In contrast, for the invisible on-shell mediator decay channel, in the $\mathcal{L}_3$ model with the fixed baseline coupling ratio $g_D/g_f = 15$, the mediator decay branching ratio $\mathcal{B}(\text{MED} \to \text{DM} + \text{DM})$ is higher than the 99% threshold set in the previous assumption, and slightly increased with the increase of M/m_D: it is 99.359% when $M/m_D = 5$, and increases to 99.399% when $M/m_D = 10$. In the $\mathcal{L}_8$ model with the fixed baseline coupling ratio $g_D/g_f = 12$, the branching ratio is also higher than the 99% threshold, showing a slight increase with the larger M/m_D: it is 99.201% when $M/m_D = 5$, and increases to 99.209% when $M/m_D = 10$. The detection efficiencies for different M/m_D values show almost no difference for the same model and mediator mass. For both the $\mathcal{L}_3$ and $\mathcal{L}_8$ models, the relative deviations of the exclusion limits for $M/m_D = 5$ and $M/m_D = 10$ with respect to the baseline $M/m_D = 2.5$ are all less than 3%.

The analysis for invisible on-shell mediator decays follows the same workflow but uses the condition $\mathcal{B}(\text{MED} \to \text{DM} + \text{DM}) > 99\%$ to prioritize DM pair production. The corresponding coupling parameter ratios g_D/g_f and $M_{D\phi}/g_f$ are listed in the fourth column of Table 17. The ratio $M_{D\phi}/g_f$ increased monotonically with the mediator mass for the fixed condition $\mathcal{B}(\text{MED} \to \text{DM} + \text{DM}) > 99\%$. Since the results depend only mildly on the M/m_D ratio once $M > 2m_D$ is satisfied, we fixed $M/m_D = 2.5$ and used the same range of benchmark mediator masses. The resulting projected exclusion limits, with and without systematic uncertainty, are shown by the solid and dashed lines in Fig. 13, respectively. In contrast to the visible decay process, the exclusion lines of the $\mathcal{L}_3$, $\mathcal{L}_4$, and $\mathcal{L}_8$ models in the invisible decay process exhibit a relatively flat trend with the increase in the mediator mass M. When systematic uncertainties are neglected (solid lines), the projected limits remain entirely below the GCE-preferred bands. For the $\mathcal{L}_9, \mathcal{L}_{10}, \mathcal{L}_{13}$, and $\mathcal{L}_{14}$ models, the exclusion lines exhibit a monotonic increase with the mediator mass M. In the lower mass regime (almost $M < 200$ GeV), the projected limits are consistently below the GCE-preferred bands, indicating a robust exclusion of the parameter space favored by the GCE explanation. However, as M increased beyond 200 GeV, the rising exclusion lines eventually surpassed the preferred bands. In this higher mass region, the GCE-favored parameter space can only be effectively probed if systematic uncertainties are neglected (as represented by the solid lines). This behavior suggests that for these specific models, a stronger exclusion of the GCE-favored regions is primarily achieved in the $M < 200$ GeV regime when systematic errors are not taken into account.

The exclusion limits derived from visible on-shell mediator decays are consistently stronger than those from invisible on-shell mediator decays across all models. This behavior can be attributed to two main factors. First, the relevant SM background for the visible decay signal process is more than an order of magnitude smaller than the invisible decay signal process. Second, although the production cross-sections for both signal processes are proportional to g_f^2, the requirement of a larger than 99% branching ratio to either $\mu^+\mu^-$ or a pair of DM particles results in distinctly different values for the coupling parameter ratios g_D/g_f and $M_{D\phi}/g_f$, as shown in Table 17.

For the mono-photon channel with an off-shell mediator, the production cross-sections are directly proportional to $g_D \cdot g_f$ for $\mathcal{L}_3$, $\mathcal{L}_4$, and $\mathcal{L}_8$ models and to $M_{D\phi} \cdot g_f$ for $\mathcal{L}_9$, $\mathcal{L}_{10}$, $\mathcal{L}_{13}$, and $\mathcal{L}_{14}$ models. We consider mass ratios $M/m_D = 1.1, 1.5, 1.9$ (satisfying $M < 2m_D$) and benchmark DM masses from 20 GeV to 100 GeV. To further evaluate the sensitivity to the GCE explanation in this context, we similarly overlay the GCE-preferred regions from Ref. [40] onto Fig. 14. The colored bands denote the favored regions for the respective models across mass ratios $M/m_D = \{1.1, 1.5, 1.9\}$. For visual clarity, we only displayed the $M/m_D = 1.1$ bands for the $\mathcal{L}_9$ and $\mathcal{L}_{10}$ models, as they fully encompass the parameter space of the higher ratios. Following a similar reason, we present only the $M/m_D = \{1.1, 1.5\}$ bands for the $\mathcal{L}_3, \mathcal{L}_4, \mathcal{L}_8$ models, and the $M/m_D = \{1.1, 1.9\}$ bands for the $\mathcal{L}_{13}, \mathcal{L}_{14}$ models. The projected exclusion limits for this scenario, without and with systematic uncertainty, are presented in Fig. 14. In contrast to the on-shell decays, the exclusion lines of all

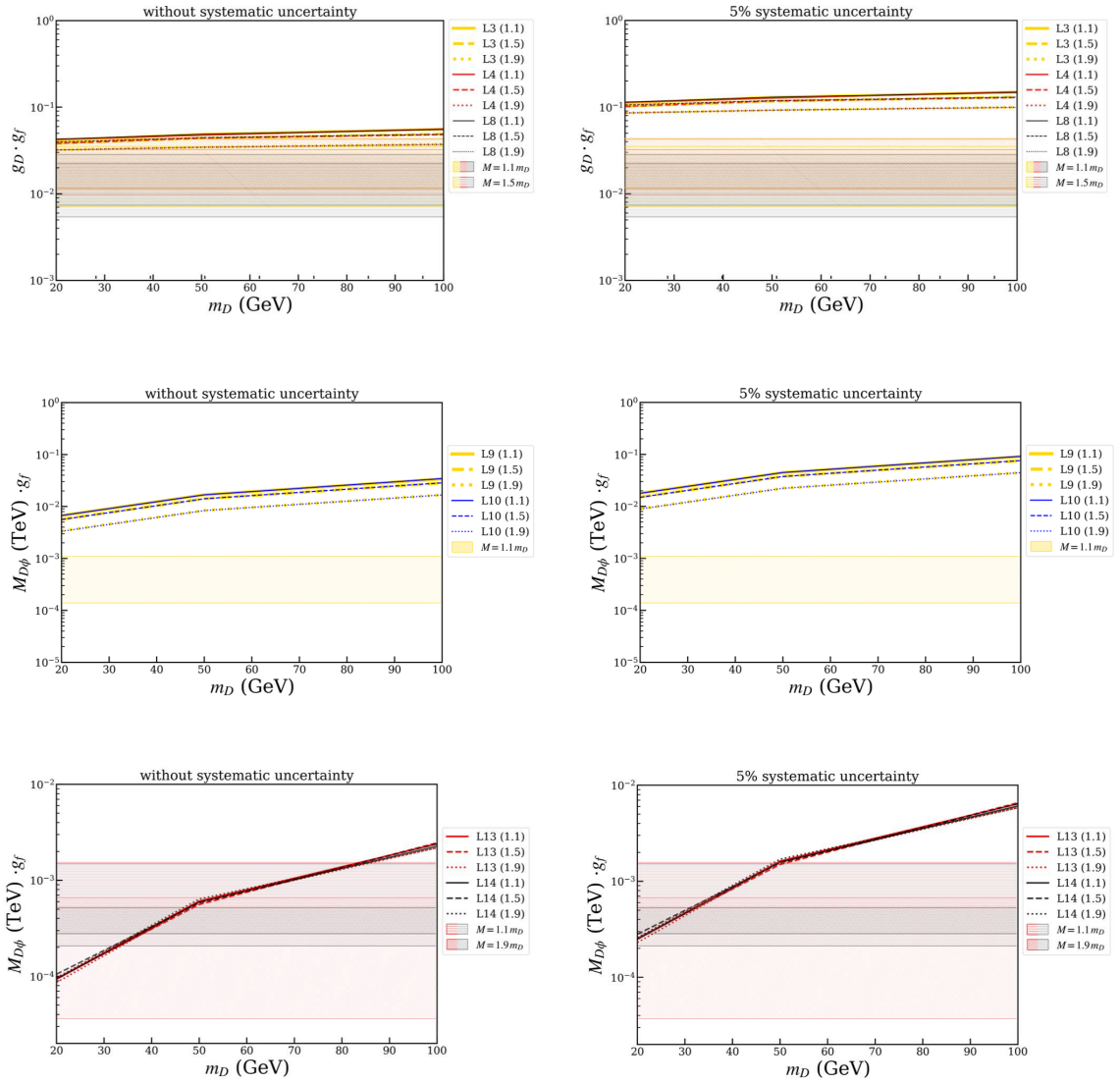

Fig. 14. (color online) Projected exclusion limits at 95% confidence level on the parameter space for mono-photon channel with an off-shell mediator in seven models without (top panels) and with a flat 5% background systematic uncertainty (bottom panels). Colored bands denote the GCE-favored parameter regions consistent with Ref. [40], where distinct colors correspond to individual models and various patterns within the bands distinguish the mediator-to-DM mass ratios M/m_D (see the main text for details).

models show a monotonic upward trend with the increase in mediator mass M. The larger the mass ratio M/m_D, the lower the exclusion lines lie, indicating higher detection sensitivity. All exclusion lines lie either above or within the GCE-preferred bands, indicating that current sensitivity remains insufficient to fully probe or constrain the parameter space favored by the GCE explanation in the off-shell regime.

The visible process exhibits a monotonically decreasing trend in the mass range 20–50 GeV, while showing a monotonically increasing trend in all other mass ranges. This is mainly due to the excessively small background cross-section and detection efficiency. In addition, under the event selection of 20 GeV (imposed by the kinematic cut on the mediator mass window), the number of background events is less than 1; hence, the process at 20 GeV is naively analyzed as a background-free process. The results of the invisible process show a monotonically increasing trend in the mass range of 50–1500 GeV. Both processes are characterized by better exclusion limits in the low- than in the high-mass range.

For the exclusion limits of the VBF process, it can be observed that for the invisible on-shell mediator decay channel, the exclusion capability of the VBF process is significantly weaker than that of the muon pair annihilation process. In contrast, for the visible on-shell mediator decay channel, the exclusion capability of the VBF process is comparable to that of the muon pair annihilation process. The core reason for this phenomenon is as follows. For the VBF process, the detection efficiencies of the signal and background are significantly different from those of the aforementioned muon pair annihilation pro-

cess. In the visible on-shell mediator decay channel, the background detection efficiency of the VBF process is more stable across different mediator mass windows, especially in the high-mass regime, where the background detection efficiency is only 1/2 to1/3 of that of the muon pair annihilation process. For the signal detection efficiency, the two processes are basically similar when the mediator mass is below 500 GeV. However, above 500 GeV, the signal detection efficiency of the VBF process is lower than that of the muon pair annihilation process, with the gap widening as the mediator mass increases. In the invisible on-shell mediator decay channel, the background detection efficiency of the VBF process is approximately twice that of the muon pair annihilation process, while there is no significant difference in the signal detection efficiency between the two processes. Although the signal cross-section of the VBF visible decay channel is lower than that of the muon pair annihilation process, the background cross-section is greatly suppressed owing to the unique four muons signature in its final state. The gain from this background suppression far outweighs the combined loss from the reduced signal cross-section and decreased signal efficiency, ultimately making its exclusion capability comparable to that of the muon pair annihilation process.

To clarify the influence of mediator decay branching ratios on detection performance, we further compared the exclusion performance characteristics at branching ratios of 90% and 50% with the case of 99% as the reference benchmark. For the visible mediator decay process, the detection sensitivity at $\mathcal{B}(\text{MED}\to\mu^+\mu^-)>50\%$ is 20 times lower than that at $\mathcal{B}(\text{MED}\to\mu^+\mu^-)>99\%$, while the detection sensitivity at $\mathcal{B}(\text{MED}\to\mu^+\mu^-)>90\%$ is 3.6 times lower than that at $\mathcal{B}(\text{MED}\to\mu^+\mu^-)>99\%$. This study explicitly states that the exclusion limits drawn for specific mediator decay channels are all based on the premise of $\mathcal{B}(\text{MED}\to\mu^+\mu^-)>99\%$.

In contrast, the exclusion limits of invisible mediator decay processes exhibit significant regularity with the variation of branching ratios: all models show the weakest exclusion performance at $\mathcal{B}(\text{MED}\to\text{DM}+\text{DM})>99\%$ and the strongest exclusion performance at $\mathcal{B}(\text{MED}\to\text{DM}+\text{DM})>50\%$. Quantitative analysis results show that the exclusion limit at $\mathcal{B}(\text{MED}\to\text{DM}+\text{DM})>90\%$ is approximately three times that at $\mathcal{B}(\text{MED}\to\text{DM}+\text{DM})>99\%$; the exclusion limit at $\mathcal{B}(\text{MED}\to\text{DM}+\text{DM})>50\%$ is approximately five times that at $\mathcal{B}(\text{MED}\to\text{DM}+\text{DM})>99\%$. For the same process and the same model, the variation trends of exclusion lines remain consistent across different mediator decay branching ratios.

In summary, the exclusion limits for the fermionic DM models with scalar or vector mediators ($\mathcal{L}_3$, $\mathcal{L}_4$, and$\mathcal{L}_8$) reached $O(10^{-5})$ for $g_D\cdot g_f$ in visible on-shell mediator decays, $O(10^{-3}-10^{-2})$ for invisible on-shell mediator decays, and $O(10^{-2}-0.1)$ for the mono-photon channel with an off-shell mediator. The projected exclusion contours covered most of the allowed nonresonance regions with $g_D\cdot g_f\gtrsim 10^{-2}$ and mediator masses M between 20 GeV and 1500 GeV for these muonphilic DM models, as shown in Ref. [40]. Similarly, for scalar DM models with a scalar mediator ($\mathcal{L}_9$, $\mathcal{L}_{10}$) and vector DM models with a scalar mediator ($\mathcal{L}_{13}$, $\mathcal{L}_{14}$), the exclusion limits on $M_{D\phi}$ (TeV)$\cdot g_f$ reached $O(10^{-6}-10^{-5})$ for visible on-shell mediator decays, $O(10^{-4}-10^{-2})$ for invisible on-shell me-

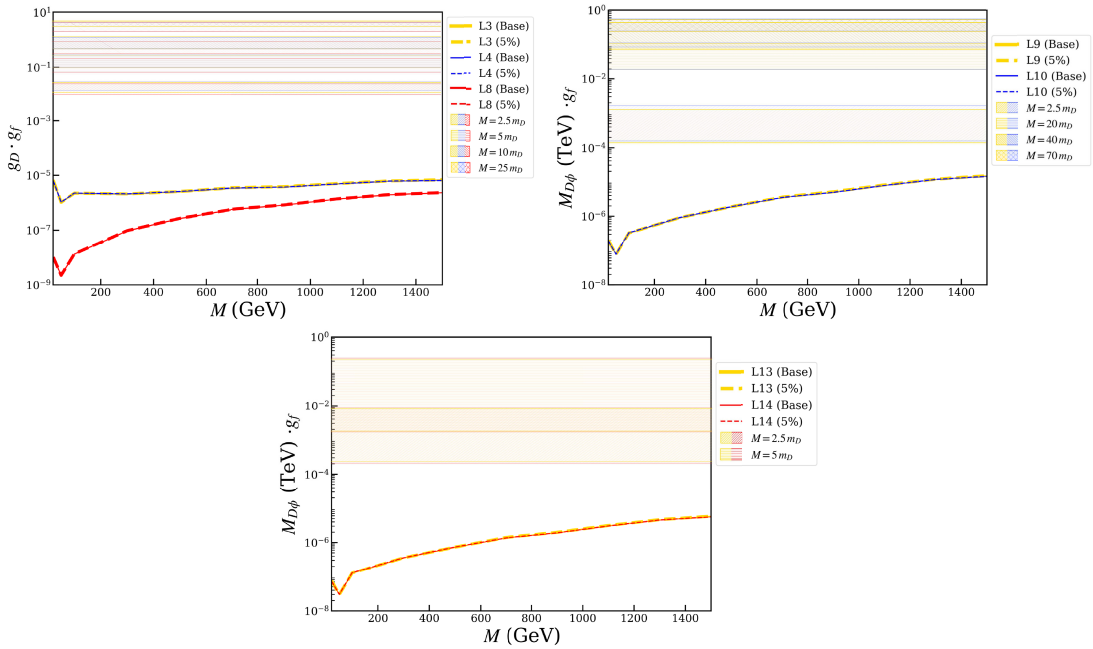

Fig. 15. (color online) Similar to Fig. 12, but for visible on-shell mediator decays via VBF process in seven models.

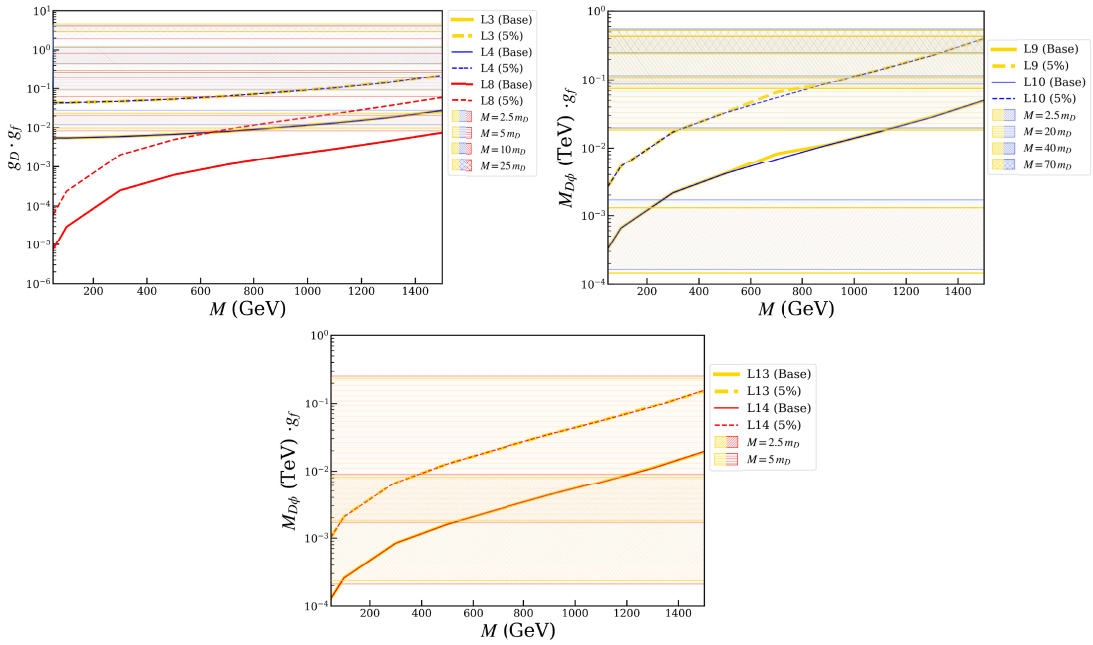

Fig. 16. (color online) Similar to Fig. 15, but for invisible on-shell mediator decays via VBF process in seven models.

diator decays, and $O(10^{-4}-10^{-2})$ for the mono-photon channel with an off-shell mediator. The projected limits covered most nonresonance regions with $M_{D\phi}\,(\mathrm{TeV})\cdot g_f \gtrsim 10^{-4}$ across the same mediator mass range. Therefore, a future 3 TeV muon collider would be critical for testing the muonphilic DM explanation of the GCE puzzle.

V. CONCLUSION

In this paper, we performed a detailed and systematic study of the prospects for discovering muonphilic DM at a future 3 TeV muon collider, focusing on simplified models with a Z_2-even mediator. Motivated by the model's ability to explain the GCE and the observed relic density while evading multimessenger, direct detection and collider constraints, we explored its viable parameter space through four distinct search channels: visible on-shell mediator decays, invisible on-shell mediator decays, mono-photon signatures with off-shell mediators, and vector boson fusion production.

Our analysis demonstrates that a muon collider possesses exceptional sensitivity to probe the nonresonant regions of these models. For visible on-shell decays, the projected exclusion limits on the fermionic DM model couplings $g_D \cdot g_f$ can reach $O(10^{-5})$, while for scalar and vector DM models, the limits on $M_{D\phi}(\mathrm{TeV})\cdot g_f$ can be as strong as $O(10^{-6}-10^{-5})$. The invisible on-shell decay channel, while slightly less sensitive owing to a larger irreducible background and coupling parameter ratios shown in Table 17, still provides powerful constraints of $O(10^{-3}-10^{-2})$ and $O(10^{-4}-10^{-2})$ for the respective model classes. The mono-photon channel with off-shell mediators offers a complementary probe, especially in parameter regions where $M < 2m_D$, with exclusion limits reaching $O(10^{-2}-0.1)$ and $O(10^{-4}-10^{-2})$. We have also quantified the impact of a conservative flat 5% systematic uncertainty, demonstrating that while it shifts the exclusion limits upward, the projected sensitivity remains substantial. This confirms the robustness of our results. The resulting exclusion contours cover most of the allowed parameter space, specifically for $g_D \cdot g_f \gtrsim 10^{-2}$ and $M_{D\phi} \cdot g_f \gtrsim 10^{-4}$TeV, across the mediator mass ranges of 20 GeV to 1.5 TeV in nonresonant regions.

In conclusion, a high-energy muon collider serves as a decisive machine to directly test the muonphilic DM hypothesis as an explanation for the GCE. Its clean collision environment and high luminosity provide a unique opportunity to perform precision measurements of the DM-muon coupling and mediator mass, directly complementing and exceeding the reach of indirect and direct detection experiments as well as conventional collider searches. Our work firmly establishes that such a facility is critical for advancing our understanding of the DM particle nature.

APPENDIX A: COLLIDER CONSTRAINTS FROM LEP AND LHC ON MUONPHILIC DM MODELS

1. LEP constraints on visible and invisible mediator decays

At the LEP, which operated at $\sqrt{s} = 209$ GeV, we focus on e^+e^- collision-induced production of the mediator

MED (denoted in the main text) for muonphilic DM models. Below, we present the detailed analysis of LEP constraints for both visible and invisible mediator decay processes.

For the visible mediator decay scenario (MED $\to \mu^+\mu^-$), the signal process is defined as

$$e^+e^- \to \mu^+\mu^-\text{MED}, \quad \text{MED} \to \mu^+\mu^-, \tag{A1}$$

and the dominant SM background process is

$$e^+e^- \to \mu^+\mu^-\mu^+\mu^-. \tag{A2}$$

Similarly, for the invisible mediator decay scenario (MED $\to$ DM + DM), the signal process is

$$e^+e^- \to \mu^+\mu^-\text{MED}, \quad \text{MED} \to \text{DM}+\text{DM}, \tag{A3}$$

and the dominant SM background process is

$$e^+e^- \to \mu^+\mu^-\nu_l\bar{\nu}_l. \tag{A4}$$

For the invisible on-shell mediator decay process, we consider the mediator mass $M = \{10, 25, 50\}$ GeV; for the visible process, the mediator masses are set to $M = \{5, 10, 25, 50\}$ GeV. With the integrated luminosity fixed at $\mathcal{L} = 233.4\ \text{pb}^{-1}$, the event selection criteria for both processes are simply optimized as detailed below:

a. Invisible Mediator Decay (MED $\to$ DM + DM)

- Cut-1 (basic cuts): $N_{\mu^+} \geq 1$, $N_{\mu^-} \geq 1$, $p_T(\mu) > 20$ GeV, $|\eta(\mu)| < 2.5$ and $\not{E}_T > 20$ GeV;
- Cut-2: $p_T(\mu_1) \geq 80$ GeV;
- Cut-3: $p_T(\mu_1)/\not{E}_T > 1.1$;

Based on these event selections, the corresponding cut-flow tables for various signal BPs in the $\mathcal{L}_9$ and $\mathcal{L}_{13}$ models as well as the background are obtained in Tables A2 and A3. It can be seen that for the invisible mediator decay process, the product of the background cross-section, integrated luminosity and detection efficiency is much less than 1. Therefore, we naively treat this analysis as a background-free scenario in the subsequent discussion.

b. Visible Mediator Decay (MED $\to \mu^+\mu^-$)

- Cut-1 (basic cuts): $N_{\mu^+} \geq 2$ and $N_{\mu^-} \geq 2$, $p_T(\mu) > 20$ GeV and $|\eta(\mu)| < 2.5$;
- Cut-2: $|M_{\mu\mu}^{\text{best}} - M| < 0.15M$

where $M_{\mu\mu}^{\text{best}}$ is defined as in the main text. For the visible mediator decay process, its background cross-section is only 2.11 fb; hence, the product of the background cross-section and integrated luminosity alone is already less than 1. Based on this, we also treat this analysis at the LEP as a background-free scenario in the subsequent discussion. Meanwhile, in the analysis of this process, we no longer apply kinematic cuts to the background nor perform relevant background analysis. Since the number of signal events passing the basic kinematic cuts is already at a low level, we only selected two kinematic cuts to filter the signal events. The cut-flow tables for the $\mathcal{L}_3$, $\mathcal{L}_8$, and $\mathcal{L}_9$ models are shown in Tables A4, A5, and A6, respectively.

Table A1. Cut-flow table for invisible on-shell mediator decay of the $\mathcal{L}_3$ model and its relevant background at the LEP. The three BPs are signal-1 ($M = 10$ GeV), signal-2 ($M = 25$ GeV), and signal-3 ($M = 50$ GeV).

	Cut description	background	signal1	signal2	signal3
	Cross-section/fb	238.10	1.20	1.64	1.41
Cut-1	$N_{\mu^+} \geq 1$, $N_{\mu^-} \geq 1$, $p_T(\mu) > 20$ GeV, $\lvert\eta(\mu)\rvert < 2.5$, $\not{E}_T > 20$ GeV	0.60	0.63	0.66	0.66
Cut-2	$p_T(\mu_1) \geq 80$ GeV, $\lvert\eta(\mu_1)\rvert < 0.8$	0.02	0.27	0.20	0.09
Cut-3	$p_T(\mu_1)/\not{E}_T > 1.1$	0.01	0.23	0.15	0.04

Table A2. Similar to Table A1, but for the $\mathcal{L}_9$ model.

	Cut description	background	signal1	signal2	signal3
	Cross-section/fb	238.10	59.39	14.15	1.18
Cut-1	$N_{\mu^+} \geq 1$, $N_{\mu^-} \geq 1$, $p_T(\mu) > 20$ GeV, $\lvert\eta(\mu)\rvert < 2.5$, $\not{E}_T > 20$ GeV	0.60	0.65	0.66	0.63
Cut-2	$p_T(\mu_1) \geq 80$ GeV, $\lvert\eta(\mu_1)\rvert < 0.8$	0.02	0.17	0.09	0.04
Cut-3	$p_T(\mu_1)/\not{E}_T > 1.1$	0.01	0.13	0.05	0.02

Table A3. Similar to Table A1, but for the $\mathcal{L}_{13}$ model.

	Cut description	background	signal1	signal2	signal3
	Cross-section/fb	238.10	28420	1028	23.54
Cut-1	$N_{\mu^+} \geq 1$, $N_{\mu^-} \geq 1$, $p_T(\mu) > 20$ GeV, $\lvert\eta(\mu)\rvert < 2.5$, $\not{E}_T > 20$ GeV	0.60	0.63	0.57	0.51
Cut-2	$p_T(\mu_1) \geq 80$ GeV, $\lvert\eta(\mu_1)\rvert < 0.8$	0.02	0.06	0.02	0.005
Cut-3	$p_T(\mu_1)/\not{E}_T > 1.1$	0.01	0.03	4.1×10^{-3}	9.0×10^{-4}

Table A4. Cut-flow table for visible on-shell mediator decay of the $\mathcal{L}_3$ model. The four BPs are signal-1 ($M = 5$ GeV), signal-2 ($M = 10$ GeV), signal-3 ($M = 25$ GeV), and signal-4 ($M = 50$ GeV).

	Cut description	signal1	signal2	signal3	signal4
	Cross-section/fb	21.56	212.10	113.40	46.29
Cut-1	$N_{\mu^+} \geq 2$ and $N_{\mu^-} \geq 2$, $p_T(\mu) > 20$ GeV, $\lvert\eta(\mu)\rvert < 2.5$	0.19	0.14	0.18	0.29
Cut-2	$\lvert M_{\mu\mu}^{\text{best}} - M\rvert < 0.15M$	0.002	0.08	0.11	0.24

Table A5. Cut-flow table for visible on-shell mediator decay of the $\mathcal{L}_8$ model. The six BPs are signal-1 ($M = 5$ GeV), signal-2 ($M = 10$ GeV), signal-3 ($M = 25$ GeV), signal-4 ($M = 50$ GeV), signal-5 ($M = 75$ GeV), and signal-6 ($M = 100$ GeV).

	Cut description	signal1	signal2	signal3	signal4	signal5	signal6
	Cross-section/fb	171.40	2538	899.10	252.40	78.24	23.32
Cut-1	$N_{\mu^+} \geq 2$, $N_{\mu^-} \geq 2$, $p_T(\mu) > 20$ GeV, $\lvert\eta(\mu)\rvert < 2.5$	0.08	0.05	0.09	0.25	0.44	0.50
Cut-2	$\lvert M_{\mu\mu}^{\text{best}} - M\rvert < 0.15M$	0.003	0.04	0.07	0.22	0.43	0.48

Table A6. Similar to Table A4, but for the $\mathcal{L}_9$ model.

	Cut description	signal1	signal2	signal3	signal4
	Cross-section/fb	286.60	212.00	113.80	46.01
Cut-1	$N_{\mu^+} \geq 2$ and $N_{\mu^-} \geq 2$, $p_T(\mu) > 20$ GeV, $\lvert\eta(\mu)\rvert < 2.5$	0.13	0.14	0.18	0.28
Cut-2	$\lvert M_{\mu\mu}^{\text{best}} - M\rvert < 0.15M$	0.09	0.10	0.13	0.24

For the $\mathcal{L}_8$ model, the number of events remains at a high level at the mediator mass of 50 GeV. Thus, we additionally analyzed two larger mediator mass BPs until the number of signal events at the corresponding mass points is no more than 3 (no exclusion capability at 95% confidence level of background-free assumption). In addition, it can be seen that in the low-mass regime, the detection efficiency after the mediator mass window cut is significantly reduced. This is because the window range corresponding to low-mass mediators is extremely small, and the number of effective events that can pass this kinematic cut is correspondingly reduced, which leads to the decrease of the detection efficiency.

Figure A1 shows the projected exclusion limits from the LEP for seven Z_2-even muonphilic DM models in the visible on-shell mediator decay channel, with the mediator mass interval covered by $M = 5-75$ GeV. For the invisible on-shell mediator decay channel, the DM mass is required to be larger than 20 GeV in our previous analysis [40]. However, our calculation shows that the parameter space with exclusion power for this process is restricted to the mediator mass interval $M \lesssim 10$ GeV. Consequently, this channel cannot impose valid exclusion constraints on the model parameter space of interest. In addition, to maintain consistency with the analysis assumptions adopted in the main text (coupling constants within a reasonable range and the mediator decay branching ratio exceeding 99%), some mass intervals are excluded from the figure as they cannot yield physically meaningful exclusion limits.

We also calculated the corresponding exclusion limits using the signal event count criterion $N_s = 10$. However, under the aforementioned analysis assumptions, except for the visible mediator decay process of the $\mathcal{L}_8$ model, other models have no valid parameter points satisfying this criterion. Thus, the results under this criterion only show the case of $N_s = 10$ for the $\mathcal{L}_8$ model in Fig. A1. The projected exclusion limits presented in this work may be optimistic compared to those from a full experimental data analysis, especially in the presence of reducible backgrounds or unaccounted detector effects.

The results show that for the visible mediator decay process, except for the $\mathcal{L}_8$ model, the LEP can only impose weak constraints on the low-mass mediator interval

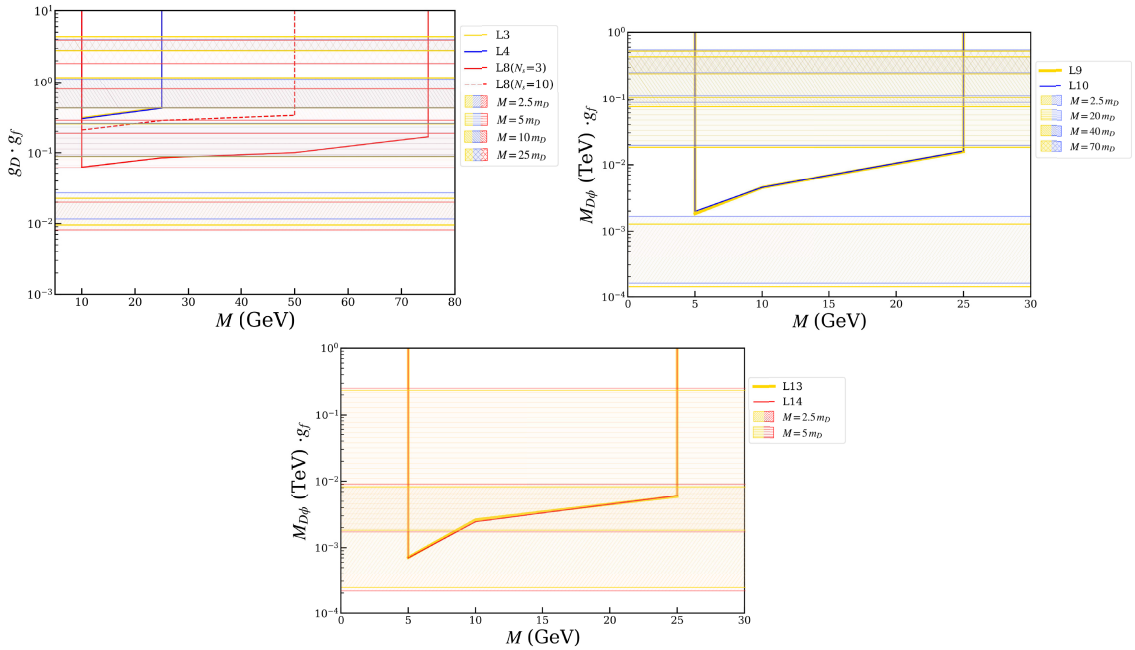

Fig. A1. (color online) Projected exclusion limits at 95% confidence level for seven models in the visible mediator decay channel at LEP, derived from a background-free assumption with the signal event count criterion $N_s = 3$, with the corresponding exclusion line for the $\mathcal{L}_8$ model under $N_s = 10$ additionally labeled.

with $M \leq 25$ GeV. For the $\mathcal{L}_8$ model, it can only provide relatively weak constraints throughout the entire covered mass interval of $10-75$ GeV. For the invisible mediator decay process, as mentioned above, the parameter space with exclusion power is available only for $M \lesssim 10$ GeV, while the DM mass is required to be larger than 20 GeV in this analysis. Therefore, none of the models have valid exclusion limits in this channel.

2. LHC constraints

For the LHC with $\sqrt{s} = 13$ TeV, a simple recasting demonstrates that it cannot impose effective constraints on the studied Z_2-even muonphilic DM models, regardless of whether the on-shell mediator undergoes visible or invisible decay processes.

To quantitatively verify the above conclusion, we first adopted the signal production cross-sections corresponding to the exclusion limits of the 2ℓ (dimuon final state) and 4ℓ (tetramuon final state) channels for the integrated luminosity $\mathcal{L} = 35.9$ fb^{-1} from Ref. [94]. For the 2ℓ channel, the mediator mass ranges from 10 to 250 GeV, with the excluded cross-section decreasing monotonically with increasing mass, spanning approximately 110–0.06 pb. For the 4ℓ channel, the mediator mass ranges from 1 to 350 GeV, and the excluded cross-section also decreases with increasing mass, from approximately 4.84 pb to 0.0028 pb. For the visible mediator decay process, the production mechanism is $pp \to \mu^+\mu^-$MED (where MED $\to \mu^+\mu^-$). For the invisible mediator decay process, the production mechanism is $pp \to \mu^+\mu^-$MED (where MED $\to$ DM + DM). For these two decay processes, 10 mediator mass BPs are selected to generate the corresponding signal cross-sections, and their orders of magnitude is quantitatively evaluated to determine whether it reached the level required for LHC constraints with $\mathcal{L} = 35.9$ fb^{-1}.

The recasting results show that for the 2ℓ channel, the signal production cross-sections of all models decreased with the increase of mediator mass, which is consistent with the variation trend of the exclusion lines in Ref. [94]. Under the assumptions that the coupling constants are within a reasonable range and the mediator decay branching ratios are greater than 99%, taking the $\mathcal{L}_3$ model as an example, for the 2ℓ channel, within the mediator mass range of 10–250 GeV, the signal production cross-section decreases from 56.76 fb to 2.57×10^{-3} fb. For the 4ℓ channel, the signal production cross-section is only 10^{-7} fb at a mediator mass of 1 GeV and 8.49×10^{-2} fb at 350 GeV. The signal production cross-sections of all intermediate mediator masses fall within this range. The above cross-section values are far lower than the reference thresholds given in Ref. [94], failing to form effective exclusion constraints. Finally, the signal production cross-sections of the remaining six models across the entire mass range do not reach the excluded levels, and none of them can be constrained by the LHC at 13 TeV with $\mathcal{L} = 35.9$ fb^{-1}. Increasing the integrated luminosity of the 13 TeV LHC is expected to yield only weak exclusion limits for the seven muonphilic DM models considered in this study.

ACKNOWLEDGMENTS

The authors gratefully acknowledge the valuable discussions and insights provided by the members of the China Collaboration of Precision Testing and New Physics.

References

[1] V. Trimble, Ann. Rev. Astron. Astrophys. **25**, 425 (1987)
[2] L. Barack, V. Cardoso, S. Nissanke *et al.*, Class. Quant. Grav. **36**(14), 143001 (2019), arXiv: 1806.05195[gr-qc]
[3] A. Arbey and F. Mahmoudi, Prog. Part. Nucl. Phys. **119**, 103865 (2021), arXiv: 2104.11488[hep-ph]
[4] M. Cirelli, A. Strumia, and J. Zupan, arXiv: 2406.01705 [hep-ph]
[5] M. Battaglieri, A. Belloni, A. Chou *et al.*, arXiv: 1707.04591 [hep-ph]
[6] T. Lin, PoS **333**, 009 (2019), arXiv: 1904.07915[hep-ph]
[7] E. G. M. Ferreira, Astron. Astrophys. Rev. **29**(1), 7 (2021), arXiv: 2005.03254[astro-ph.CO]
[8] A. Belenchia, M. Carlesso, Ö. Bayraktar *et al.*, Phys. Rept. **951**, 1 (2022), arXiv: 2108.01435[quant-ph]
[9] C. Pérez de los Heros, Symmetry **12**(10), 1648 (2020), arXiv: 2008.11561[astro-ph.HE]
[10] T. R. Slatyer, SciPost Phys. Lect. Notes **53**, 1 (2022), arXiv: 2109.02696[hep-ph]
[11] I. Cholis, Y. M. Zhong, S. D. McDermott *et al.*, Phys. Rev. D **105**(10), 103023 (2022), arXiv: 2112.09706[astro-ph.HE]
[12] M. Di Mauro and M. W. Winkler, Phys. Rev. D **103**(12), 123005 (2021), arXiv: 2101.11027[astro-ph.HE]
[13] M. Y. Cui, Q. Yuan, Y. L. S. Tsai *et al.*, Phys. Rev. Lett. **118**(19), 191101 (2017), arXiv: 1610.03840[astro-ph.HE]
[14] A. Cuoco, M. Krämer, and M. Korsmeier, Phys. Rev. Lett. **118**(19), 191102 (2017), arXiv: 1610.03071[astro-ph.HE]
[15] F. Calore, M. Cirelli, L. Derome *et al.*, SciPost Phys. **12**(5), 163 (2022), arXiv: 2202.03076[hep-ph]
[16] C. A. Kierans, S. E. Boggs, A. Zoglauer *et al.*, Astrophys. J. **895**(1), 44 (2020), arXiv: 1912.00110[astro-ph.HE]
[17] R. G. Cai, Y. C. Ding, X. Y. Yang *et al.*, JCAP **03**, 057 (2021), arXiv: 2007.11804[astro-ph.CO]
[18] C. Keith and D. Hooper, Phys. Rev. D **104**(6), 063033 (2021), arXiv: 2103.08611[astro-ph.CO]
[19] E. M. Silich, K. Jahoda, L. Angelini *et al.*, Astrophys. J. **916**(1), 2 (2021), arXiv: 2105.12252[astro-ph.HE]
[20] D. Hooper and T. R. Slatyer, Phys. Dark Univ. **2**, 118 (2013), arXiv: 1302.6589[astro-ph.HE]
[21] L. Goodenough and D. Hooper, arXiv: 0910.2998 [hep-ph]
[22] D. Hooper and L. Goodenough, Phys. Lett. B **697**, 412 (2011), arXiv: 1010.2752[hep-ph]
[23] M. Ajello *et al.* (Fermi-LAT), Astrophys. J. **819**(1), 44 (2016), arXiv: 1511.02938[astro-ph.HE]
[24] J. F. Navarro, C. S. Frenk, and S. D. M. White, Astrophys. J. **462**, 563 (1996), arXiv: astro-ph/9508025[astro-ph]
[25] A. McDaniel, T. Jeltema, S. Profumo *et al.*, JCAP **09**, 027 (2017), arXiv: 1705.09384[astro-ph.HE]
[26] T. E. Jeltema and S. Profumo, Mon. Not. Roy. Astron. Soc. **421**, 1215 (2012), arXiv: 1108.1407[astro-ph.HE]
[27] M. J. Dolan, F. Kahlhoefer, C. McCabe *et al.*, JHEP **03**, 171 (2015) [Erratum: JHEP **07**, 103 (2015)]., arXiv: 1412.5174[hep-ph]
[28] S. Ipek, D. McKeen, and A. E. Nelson, Phys. Rev. D **90**(5), 055021 (2014), arXiv: 1404.3716[hep-ph]
[29] A. Berlin, D. Hooper, and S. D. McDermott, Phys. Rev. D **89**(11), 115022 (2014), arXiv: 1404.0022[hep-ph]
[30] A. Alves, S. Profumo, F. S. Queiroz *et al.*, Phys. Rev. D **90**(11), 115003 (2014), arXiv: 1403.5027[hep-ph]
[31] P. Agrawal, B. Batell, D. Hooper *et al.*, Phys. Rev. D **90**(6), 063512 (2014), arXiv: 1404.1373[hep-ph]
[32] E. Izaguirre, G. Krnjaic, and B. Shuve, Phys. Rev. D **90**(5), 055002 (2014), arXiv: 1404.2018[hep-ph]
[33] P. Ko, W. I. Park, and Y. Tang, JCAP **09**, 013 (2014), arXiv: 1404.5257[hep-ph]
[34] M. Abdullah, A. DiFranzo, A. Rajaraman *et al.*, Phys. Rev. D **90**, 035004 (2014), arXiv: 1404.6528[hep-ph]
[35] A. Martin, J. Shelton, and J. Unwin, Phys. Rev. D **90**(10), 103513 (2014), arXiv: 1405.0272[hep-ph]
[36] A. Berlin, P. Gratia, D. Hooper *et al.*, Phys. Rev. D **90**(1), 015032 (2014), arXiv: 1405.5204[hep-ph]
[37] C. Cheung, M. Papucci, D. Sanford *et al.*, Phys. Rev. D **90**(7), 075011 (2014), arXiv: 1406.6372[hep-ph]
[38] P. Agrawal, B. Batell, P. J. Fox *et al.*, JCAP **05**, 011 (2015), arXiv: 1411.2592[hep-ph]
[39] C. Karwin, S. Murgia, T. M. P. Tait *et al.*, Phys. Rev. D **95**(10), 103005 (2017), arXiv: 1612.05687[hep-ph]
[40] M. Abdughani, Y. Z. Fan, C. T. Lu *et al.*, JHEP **07**, 127 (2022), arXiv: 2111.02946[astro-ph.HE]
[41] Y. Z. Fan, T. P. Tang, Y. L. S. Tsai *et al.*, Phys. Rev. Lett. **129**(9), 091802 (2022), arXiv: 2204.03693[hep-ph]
[42] Y. Z. Fan, Y. Y. Li, C. T. Lu *et al.*, Phys. Rev. D **111**(1), 015046 (2025), arXiv: 2410.00638[hep-ph]
[43] M. Aguilar *et al.* (AMS), Phys. Rev. Lett. **117**(9), 091103 (2016)
[44] M. Aguilar *et al.* (AMS), Phys. Rev. Lett. **122**(4), 041102 (2019)
[45] Z. Bo *et al.* (PandaX), Phys. Rev. Lett. **134**(1), 011805 (2025), arXiv: 2408.00664[hep-ex]
[46] G. Krnjaic, G. Marques-Tavares, D. Redigolo *et al.*, Phys. Rev. Lett. **124**(4), 041802 (2020), arXiv: 1902.07715[hep-ph]
[47] R. Garani and J. Heeck, Phys. Rev. D **100**(3), 035039 (2019), arXiv: 1906.10145[hep-ph]
[48] B. D. Sáez and K. Ghorbani, Phys. Lett. B **823**, 136750 (2021), arXiv: 2107.08945[hep-ph]
[49] M. Drees and W. Zhao, Phys. Lett. B **827**, 136948 (2022), arXiv: 2107.14528[hep-ph]
[50] T. Hapitas, D. Tuckler, and Y. Zhang, Phys. Rev. D **105**(1), 016014 (2022), arXiv: 2108.12440[hep-ph]
[51] D. Borah, M. Dutta, S. Mahapatra *et al.*, Phys. Rev. D **105**(1), 015029 (2022), arXiv: 2109.02699[hep-ph]
[52] A. D. Medina, N. I. Mileo, A. Szynkman *et al.*, Phys. Rev. D **106**(7), 075018 (2022), arXiv: 2112.09103[hep-ph]
[53] J. Heeck and A. Thapa, Eur. Phys. J. C **82**(5), 480 (2022), arXiv: 2202.08854[hep-ph]
[54] S. Baek, J. Kim, and P. Ko, JHEP **01**, 014 (2025), arXiv: 2204.04889[hep-ph]
[55] C. A. Manzari, J. Martin Camalich, J. Spinner *et al.*, Phys. Rev. D **108**(10), 10 (2023), arXiv: 2307.03143[hep-ph]
[56] P. Figueroa, G. Herrera, and F. Ochoa, Phys. Rev. D **110**(9), 095018 (2024), arXiv: 2404.03090[hep-ph]

[57] H. Li, Z. Liu, and N. Song, arXiv: 2501.06294 [hep-ph]
[58] Z. W. Wang, Z. L. Han, F. Huang *et al*., Phys. Rev. D **111**(9), 095017 (2025), arXiv: 2501.08622[hep-ph]
[59] T. P. Tang, M. Yang, K. K. Duan *et al*., JCAP **11**, 013 (2025), arXiv: 2505.05359[hep-ph]
[60] N. F. Bell, G. Busoni, and A. Ghosh, JCAP **10**, 060 (2025), arXiv: 2505.06506[hep-ph]
[61] B. De, arXiv: 2509.10939 [hep-ph]
[62] G. Elor, N. L. Rodd, T. R. Slatyer *et al*., JCAP **06**, 024 (2016), arXiv: 1511.08787[hep-ph]
[63] M. Di Mauro, Phys. Rev. D **103**(6), 063029 (2021), arXiv: 2101.04694[astro-ph.HE]
[64] R. M. Crocker, N. F. Bell, C. Balazs *et al*., Phys. Rev. D **81**, 063516 (2010), arXiv: 1002.0229[hep-ph]
[65] M. H. Chan, Astrophys. Space Sci. **362**(9), 147 (2017), arXiv: 1707.00388[astro-ph.HE]
[66] D. Hooper, A. V. Belikov, T. E. Jeltema *et al*., Phys. Rev. D **86**, 103003 (2012), arXiv: 1203.3547[astro-ph.CO]
[67] J. de Blas *et al.* (Muon Collider), arXiv: 2203.07261 [hep-ph]
[68] K. M. Black, S. Jindariani, D. Li *et al*., JINST **19**(02), T02015 (2024), arXiv: 2209.01318[hep-ex]
[69] C. Accettura, D. Adams, R. Agarwal *et al*., Eur. Phys. J. C **83**(9), 864 (2023) [Erratum: Eur. Phys. J. C **84**(1), 36 (2024)], arXiv: 2303.08533[physics.acc-ph]
[70] J. M. Cline, G. Dupuis, Z. Liu *et al*., JHEP **08**, 131 (2014), arXiv: 1405.7691[hep-ph]
[71] M. Carena, J. Osborne, N. R. Shah *et al*., Phys. Rev. D **100**(5), 055002 (2019), arXiv: 1905.03768[hep-ph]
[72] J. Koechler and M. Di Mauro, arXiv: 2508.02775 [hep-ph]
[73] Y. Hu, C. Cesarotti, and T. R. Slatyer, arXiv: 2509.08043 [hep-ph]
[74] P. A. R. Ade *et al*. (Planck), Astron. Astrophys. **594**, A13 (2016), arXiv: 1502.01589[astro-ph.CO]
[75] Y. Meng *et al*. (PandaX-4T), Phys. Rev. Lett. **127**(26), 261802 (2021), arXiv: 2107.13438[hep-ex]
[76] A. Heister *et al*. (ALEPH), Phys. Lett. B **533**, 223 (2002), arXiv: hep-ex/0203020[hep-ex]
[77] B. Abi *et al*. (Muon g-2), Phys. Rev. Lett. **126**(14), 141801 (2021), arXiv: 2104.03281[hep-ex]
[78] P. J. Fox, R. Harnik, J. Kopp *et al*., Phys. Rev. D **84**, 014028 (2011), arXiv: 1103.0240[hep-ph]
[79] P. J. Fox, R. Harnik, J. Kopp *et al*., Phys. Rev. D **85**, 056011 (2012), arXiv: 1109.4398[hep-ph]
[80] J. P. Lees *et al*. (BaBar), Phys. Rev. D **94**(1), 011102 (2016), arXiv: 1606.03501[hep-ex]
[81] I. Adachi *et al*. (Belle-II), Phys. Rev. D **109**(11), 112015 (2024), arXiv: 2403.02841[hep-ex]
[82] Y. M. Andreev *et al*. (NA64), Phys. Rev. Lett. **132**(21), 211803 (2024), arXiv: 2401.01708[hep-ex]
[83] Y. M. Andreev *et al*. (NA64), Phys. Rev. D **110**(11), 112015 (2024), arXiv: 2409.10128[hep-ex]
[84] C. Y. Chen, J. Kozaczuk, and Y. M. Zhong, JHEP **10**, 154 (2018), arXiv: 1807.03790[hep-ph]
[85] A. Alloul, N. D. Christensen, C. Degrande *et al*., Comput. Phys. Commun. **185**, 2250 (2014), arXiv: 1310.1921[hep-ph]
[86] J. Alwall, R. Frederix, S. Frixione *et al*., JHEP **07**, 079 (2014), arXiv: 1405.0301[hep-ph]
[87] T. Sjöstrand, S. Ask, J. R. Christiansen *et al*., Comput. Phys. Commun. **191**, 159 (2015), arXiv: 1410.3012[hep-ph]
[88] J. de Favereau *et al*. (DELPHES 3), JHEP **02**, 057 (2014), arXiv: 1307.6346[hep-ex]
[89] J. P. Delahaye, M. Diemoz, K. Long *et al*., arXiv: 1901.06150 [physics.acc-ph]
[90] K. Long, D. Lucchesi, M. Palmer *et al*., Nature Phys. **17**(3), 289 (2021), arXiv: 2007.15684[physics.acc-ph]
[91] A. L. Read, J. Phys. G **28**, 2693 (2002)
[92] A. Arhrib, K. Cheung, and C. T. Lu, Phys. Rev. D **102**(9), 095026 (2020), arXiv: 1910.02571[hep-ph]
[93] K. Cheung and C. J. Ouseph, Phys. Rev. D **108**(3), 035003 (2023), arXiv: 2303.16514[hep-ph]
[94] M. Drees, M. Shi, and Z. Zhang, Phys. Lett. B **791**, 130 (2019), arXiv: 1811.12446[hep-ph]